Statistical Dynamical Systems of Flaky Particles Suspended in a Two-Dimensional Incompressible Fluid and Their Neural Network Modeling

Isshin Arai[1]*, Tomoaki Itano[2], and Masako Sugihara-Seki[2]

[1] *Graduate School of Sience and Engineering, Kansai University, Osaka, 564-8680, Japan*
[2] *Department of Pure and Applied Physics, Faculty of Engineering Science, Kansai University, Osaka, 564-8680, Japan*

In optical visualization experiments using flakey particles, the relationship between the resulting brightness patterns and the flow field is complex, and numerous studies have been conducted to explore this connection, for example G. Gauthier, P. Gondret, and M. Rabaud, Physics of Fluids, vol.10, no.9, pp.2147-2154, 1998. We present a dynamical system model for the orientation distribution of flakey particles floating in an incompressible Newtonian fluid. Optical flow visualization using flakey particles is closely related to the orientation dyanmics described by multiple points moving on a unit sphere, which is goverened under the shear history experienced by an infinitesimal flakey particle drifting in the flow. Although these points move individually on the unit sphere according to the flow field, quantitatively evaluating the time-dependent flow information obtained via visualization is generally challenging. To address this difficulty, we project the set of points on the unit sphere into a three-dimensional space determined by the particle trajectories so that we can gain insight into flow-visualization experiments. Additionally, we employ a simple neural network model to characterize the dynamics, which are not necessarily closed, in this three-dimensional space. Our approach provides a new perspective for understanding the relationship between distribution states and their governing principles, offering potential applications not only in fluid dynamics but also in visualization techniques and data-driven modeling in related fields.

1. Introduction

Optical visualization using flakey particles and coated mica particles has been established as an effective technique for the experimental characterization of incompressible Newtonian

---

*k078403@kansai-u.ac.jp

fluids.[1,2] Gauthier et al.[3] investigated the orientation trajectories of elliptical particles in a three-dimensional flow and demonstrated the consistency between experimental observations and numerical predictions based on Jeffery's solution[4] within a Taylor—Couette flow. It is well-established that particles with a sufficiently small Stokes number follow fluid motion and maintain a uniform spatial distribution. These particles undergo orientation changes in response to an imposed shear field, and their rotational motion is described by Jeffery's solution.[4] Specifically, ellipsoidal particles of finite thickness exhibit continuous rotational motion with a finite period, whereas idealized particles of negligible thickness tend to align preferentially in the principal shear direction. Notably, flakey particles such as aluminum flakes, which are commonly employed in flow visualization experiments, may be approximated as zero-thickness particles. Flow visualization experiments are representative cases in which this alignment phenomenon manifests. Based on Jeffery's solution, Savas[5] analyzed the oriented probability density distribution on parallel flows, the flow over a rotating disk, and the spinup from rest in a cylindrical cavity by considering a local flow. Predictions were made for parallel flow, flow on a rotating disk, flow in a cylindrical cavity, so that the predicted brightness pattern was experimentally confirmed. Flakey particles may serve as effective probes for extracting structural information from the flow field through a shear-induced orientation alignment. However, in practical experimental systems, these particles possess finite thicknesses and are influenced by thermal disturbances such as Brownian motion. The *particle orientation distribution* (POD) refers to the orientation distribution of a flakey fluid element drifting in the flow. Even under idealized conditions, wherein POD gradually converges toward the principal shear direction, this convergence may be disrupted by shape anisotropy or thermal fluctuations. Kida[6] formulated an orientation equation for flakey particles that explicitly accounts for Brownian motion, thereby quantifying the extent to which thermal factors contribute to the POD isotropy.

In visualization experiments, light from the illumination source is reflected by the flakey particles and captured by a camera, with the resulting orientation bias manifesting as an optical signal. Goto et al.[7] successfully visualized eddy structures in turbulence using flakey particles, as this results is attributed to the convergence of the POD over time. Specifically, even if the initial particle orientations are isotropically distributed within an infinitesimally small region, the drift leads to the emergence of anisotropy, ultimately resulting in alignment. The aligned particles reflect the incident light in a specific direction, rendering the structural features of the flow field discernible. The convergence of the POD serves as a fundamental mechanism for interpreting flow structures.

However, the convergence of the POD is not necessarily guaranteed across all flow fields. The history of the shear experienced by a particle plays a crucial role in determining its orientation dynamics, reflecting the residual effects of past flow conditions on its current state. Any arbitrary flow field can be locally approximated as a sum of strain and rotation, such that the cumulative history of shear experienced by the particles is not represented only by a simple addition of parallel shears. Under conditions that cannot be approximated by parallel shears, the interpretation of brightness patterns, not only in time-dependent flow visualization but also in steady flow visualization, becomes significantly complex, posing challenges in extracting detailed flow structures.

Egbers et al.[8)] used aluminum flakes as tracer particles to visualize flow in the early stages of transition in a spherical Couette flow (SCF). Yoshikawa et al.[9)] and Arai et al.[10)] investigated the visualization of flow by suspending aluminum flakes in the m-fold spiral state of an SCF. Numerical simulations successfully reproduced the experimental visualization results, revealing that the POD does not converge in the spiral state, even under idealized conditions where the effects of particle shape and Brownian motion are neglected. However, the spiral state and wavenumber can be successfully identified by leveraging the periodicity of the luminance pattern. Furthermore, numerical simulations using a two-dimensional model have demonstrated that the periodicity and wavenumber of the flow can be extracted from the collective orientation behavior of suspended flakey particles.[11)] Thus, the visualization of flakey particles has been widely applied in various contexts. However, the correlation between the POD and the flow field has been quantitatively evaluated only for a few limited cases of flow fields. Moreover, determining the flow information represented by the brightness patterns obtained through visualization, which is closely related to the POD, remains a significant challenge.

Here, we propose a novel index for quantifying the collective or stochastic nature of the POD and its correlation with the underlying flow field in a time-dependent two-dimensional flow. In this study, the orientation changes of flakey particles suspended in an incompressible Newtonian fluid are considered from a set-theoretical perspective, thereby formulating the dynamics of the three indicators I, O, P in the *shear history space*. Here, the first indicator, I, represents the anisotropy of POD, while the second and third indicator, O and P, quantify the relationship between the POD and the flow field. This approach offers a new framework for understanding the relationship among the flow field, POD, and observed patterns. Furthermore, we elucidate the existence of attractors, limit cycles, periodic orbits, and turbulent-like behavior within the shear history space. However, we also show it is impossible to extract the flow-shear information through visualization in general flow fields, even if eliminating isotropic mechanisms such as particle shape effects and thermal fluctuations.

First, a set-theoretic description is provided in Section 2 to quantitatively evaluate the relationship between the POD and flow. We then apply the introduced concept to a model presented in Section 3. Based on the results, we analyze the shear history space from the perspective of the visualization experimenter in Section 4-1. Finally, In Section 4-2, we employ weak modeling using neural network to analyze the dynamics that are not necessarily closed within the shear history space. Finally, In Section 5, This approach enables us to capture the intricate relationship between the POD and shear flow, which conventional analytical methods fail to describe fully. Ultimately, our study offers a new perspective for quantifying the information retrievable from flow visualization.

2. Set-theoretic description of POD

Let the translational motion of flakey particles suspended in an incompressible Newtonian fluid be governed by the following equation:

$$\frac{d\boldsymbol{r}}{dt} = \boldsymbol{u}(\boldsymbol{r}). \tag{1}$$

where $\boldsymbol{r}$ is the position of the particle and $\boldsymbol{u}(\boldsymbol{r})$ is the velocity at position $\boldsymbol{r}$. According to Ref.13), the time evolution of the unit normal vector $\boldsymbol{s}$ of the flakey particles is assumed to be described by the following equation:

$$\frac{d\boldsymbol{s}}{dt} = \boldsymbol{s} \times \boldsymbol{s} \times (\boldsymbol{\nabla u}(\boldsymbol{r}) \cdot \boldsymbol{s}). \tag{2}$$

The solution to this equation is equivalent to that derived by neglecting thickness in Jeffery's solution under the assumption of infinitesimally small particles. The equation for the microfacial element of a fluid as described by Batchelor[12)] indicates that flakey particles stick to the fluid elements and are in rotational motion. Thermal effects are disregarded in relation to both the translational and rotational motions of the particles.

The change in orientation $\boldsymbol{s}$ can be conceptualized as the motion of a point on a unit sphere. Thus, $\boldsymbol{s}$ is redefined as a unit vector representing a point on the unit sphere. Let $\mathfrak{S}$ be a set consisting of all points on a sphere. Eq. (2) shows that the velocity gradient tensor uniquely determines the motion of point $\boldsymbol{s}$. For any $\boldsymbol{s}$, we define the mapping f from the set $\mathcal{D}$ consisting of all velocity gradient tensors to the tangent vector space $\mathcal{F}$ on the unit sphere as follows:

$$f : \boldsymbol{s} \times \boldsymbol{s} \times (\nabla \boldsymbol{u} \cdot \boldsymbol{s}) \quad \text{for } \nabla \boldsymbol{u} \in \mathcal{D}. \tag{3}$$

This mapping is injective but not surjective, and the inverse mapping is not well-defined in general. However, provided that a given tangent vector field $\dot{\boldsymbol{s}}(\boldsymbol{s})$ on the unit sphere is guaranteed to be obtained based on the aforementioned equation from some velocity gradient tensor, then a unique $\boldsymbol{\nabla u}$ should be determined from the tangent vector field. This can be proven using the method of contradiction. Suppose that the tangent vector field calculated from two different velocity gradient tensors $[\boldsymbol{\nabla u}]_1$ and $[\boldsymbol{\nabla u}]_2$ is identical. Then $\boldsymbol{s}\times\boldsymbol{s}\times([\boldsymbol{\nabla u}]_2-[\boldsymbol{\nabla u}]_1)\cdot\boldsymbol{s} = 0$ holds for any $\boldsymbol{s}$. Therefore, $\boldsymbol{s}\times([\boldsymbol{\nabla u}]_2-[\boldsymbol{\nabla u}]_1)\cdot\boldsymbol{s}//\boldsymbol{s}$ holds only if $([\boldsymbol{\nabla u}]_2-[\boldsymbol{\nabla u}]_1)\cdot\boldsymbol{s} = 0$ is the case. Thus, $([\boldsymbol{\nabla u}]_2-[\boldsymbol{\nabla u}]_1)$ must be a constant multiple of the unit tensor. From the incompressibility condition, the constant must be 0, leading to the conclusion that $[\boldsymbol{\nabla u}]_2 = [\boldsymbol{\nabla u}]_1$, which contradicts our initial assumption.

When an arbitrary POD is considered, we define the *state space* $\mathbb{J}$ (FIG.1) as a subset of $\mathfrak{S}$, consisting of a finite number of points on the unit spheres ($\mathbb{J} \subset \mathfrak{S}$ and $\mathbb{J} \in \mathfrak{J}$). To describe how the state space evolves over time with the flow field, we let the state space $\mathbb{J}$ move (float) in a flow $\mathbb{U} \in \mathfrak{U}$, where $\mathbb{U}$ may be time-varying. Let the path of motion of $\mathbb{J}$ start from $\boldsymbol{r}_0 = \boldsymbol{r}(t_0)$, i.e., the trajectory of a particle be defined as $\mathbb{T}_{\mathbb{U},\boldsymbol{r}_0} = \{\boldsymbol{r}(t) \mid t \in [t_0, \infty)\}$, and let $\mathfrak{T}$ be the set from which all trajectories originate. The subset $\mathfrak{t} = \{\boldsymbol{r}(t) \mid t \in [t_0, t_T]\}$, obtained by segmenting the trajectory $\mathbb{T}_{\mathbb{U},\boldsymbol{r}_0}$ over a given time interval, is projected onto $\mathbb{D} = \{\nabla\boldsymbol{u}(t) \mid t \in [t_0, t_T]\}$ via the mapping $d_{\mathbb{U}}$, which is determined by $\mathbb{U}$. This mapping is not solely determined by the trajectory $\mathfrak{t}$ but also depends on $\mathbb{U}$ itself. Here, $\mathbb{D}$ belongs to the collection $\mathfrak{D}_{\mathbb{U}}$, where $\mathfrak{D}_{\mathfrak{U}}$ consists of all elements $\mathbb{D}$.

We also denote the *shear history* in which the state space undergoes drift as $\mathbb{SH} = \{f(t) \mid t \in [t_0, t_T]\}$. Here, $f(t) \in \mathcal{F}$, and $f(t)$ can also be thought of as a map $g \in G$ projecting one state space $\mathbb{J}_1$ onto another state space $\mathbb{J}_2$, where G represents the set of all maps $g : \mathbb{J}_1 \mapsto \mathbb{J}_2$ for $\mathbb{J}_1, \mathbb{J}_2 \in \mathfrak{J}$. Let $\mathfrak{S}\mathfrak{H}_{\mathbb{U}}$ be the set of elements of $\mathbb{SH}$ in $\mathbb{U}$. From the relationship between $\mathcal{F}$ and $\mathcal{D}$, there exists a mapping from $\mathfrak{D}_{\mathbb{U}}$ to $\mathfrak{S}\mathfrak{H}_{\mathbb{U}}$. Then, we define a map h such that $h : \mathbb{SH} \mapsto g$ for $\mathbb{SH} \in \mathfrak{S}\mathfrak{H}_{\mathbb{U}}, g \in G$. In this case, map g functions as $g : \mathbb{J}_{t_0} \mapsto \mathbb{J}_{t_T}$ for $\mathbb{J}_{t_0}, \mathbb{J}_{t_T} \in \mathfrak{J}$.

1 For a given flow $\mathbb{U}$, define the initial position $\boldsymbol{r}_0 = \boldsymbol{r}(t_0)$.

2 The shear history $\mathbb{SH}$ is extracted from the path $\mathfrak{t} \subset \mathbb{T}_{\mathbb{U},\boldsymbol{r}_0}$ up to time t_T.

3 The extracted shear history is transformed into g via the map h.

4 The state space $\mathbb{J}_{t_0}$ at time t_0 is projected onto the state space $\mathbb{J}_{t_T} = \mathbb{J}_{\mathbb{SH}}$ at time t_T through the map g.

We consider the orientation of flakey particles suspended in a plane Couette flow. It is

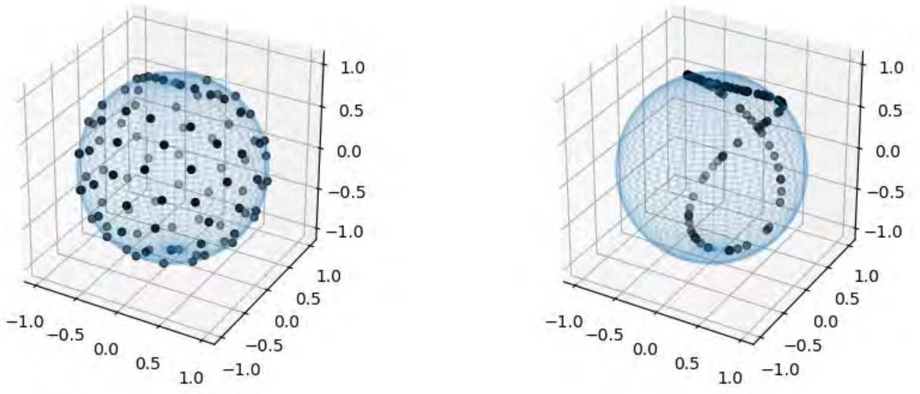

Fig. 1. Examples of the state space $\mathbb{J}$, which is formed by $N = 100$ points distributed on a unit sphere, illustrating their spatial configuration.

possible that the normal vector of the flakey particles converges to a state perpendicular to the streamline. When the thickness of the particles is non-zero, a periodic rotational behavior is observed; however, in the case of zero thickness, no rotational behavior occurs. This behavior is also evident from Eq.2. In a plane Couette flow, any state space $\mathbb{J} \in \mathfrak{J}$ is mapped to the set representing the unidirectional $\mathbb{J} \in \mathfrak{J}_{unidirection}$ by a mapping g derived from the shear history set $\mathfrak{SH}_{couette}$. The state space $\mathbb{J} \in \mathfrak{J}$ is a state space in which a finite number of points on a unit sphere are gathered at a certain point. Here, $\mathfrak{SH}_{couette}$ represents the shear history in a plane Couette flow and is a subset of $\mathfrak{SH}$. Additionally, $\mathfrak{J}_{unidirection}$ is a subset of $\mathfrak{J}$. In other words, a sufficiently long path $\mathrm{t} \subset \mathbb{T}_{couette,\boldsymbol{r}_0} \in \mathfrak{T}_{couette}$ provides $\mathbb{SH} \in \mathfrak{SH}_{couette}$, and as a result, $\mathbb{J} \in \mathfrak{J}$ converges to $\mathbb{J}_{\mathbb{SH}} \in \mathfrak{J}_{unidirection}$.

To quantitatively evaluate a state space $\mathbb{J}$, we introduce a surjective map $i : \mathbb{J} \mapsto I$ ($\mathbb{J} \in \mathfrak{J}$, $I \in \mathbb{I}$). Here, $\mathbb{I}$ is defined as the real interval $[0, 1]$ and the map is defined such that for the attractor state space, $i(\mathbb{J}) = 1$. The map i projects the set of state spaces $\mathfrak{J}$ onto the real set $\mathbb{I} \subset [0, 1]$, thereby quantifying the POD state.

Let us consider a visualization experiment in a plane Couette flow. It is expected that suspending flakey particles and placing light sources in two orthogonal directions will provide a good understanding of the flow field. This is because the light from the direction perpendicular to the plates is reflected at an angle of 0, whereas the light from the direction parallel to the plates passes through the fluid and is not reflected (here, the effect of light refraction is neglected). The POD, i.e., the state space $\mathbb{J}$, converges when $i(\mathbb{J}) = 1$, where the normal vectors of the flakey particles are perpendicular to the streamline. Consequently, visualization can be used to provide an overview of the flow field. Thus, to obtain an outline of the flow, such as the shear direction, it is desirable that $\mathbb{J} \in \mathfrak{J}_{unidirection}$, indicating $i(\mathbb{J}) = 1$. However, even if $\mathbb{J} \in \mathfrak{J}_{unidirection}$, we cannnot expect direct access to flow information. This is because $I \in \mathbb{I}$ does not contain information regarding the normal vectors of particles perpendicular to the streamline. This implies that even if all flakey particles are oriented in the same direction, the process of acquiring flow information or its methods is not simplified.

Let i be a mapping that allows us to project the state space $\mathbb{J}$ onto a real number I. However, I does not retain complete information regarding the flow field and history, such as $\mathbb{SH}$. Therefore, even if $\mathbb{J} \in \mathfrak{J}_{unidirection}$ (i.e., $i(\mathbb{J}) = 1$), reconstructing the details of the flow field may be difficult. To address this issue, we introduce two new sets: $\mathbb{O}$ and $\mathbb{P}$.

First, we consider the surjection $o : \mathbb{J} \mapsto O$ for $\mathbb{J} \in \mathfrak{J}$ and $O \in \mathbb{O}$. Here, $\mathbb{O}$ denotes the real interval $[0, 1]$. For example, if the main shear direction of the flow field is used, we obtain O by analyzing the relationship between the finite points in $\mathbb{J}$ and a reference point on the unit sphere. This mapping allows us to obtain information regarding the characteristics of the state space $\mathbb{J}$ relative to the flow field. However, because mapping o is not bijective, some information about the state space $\mathbb{J}$ is lost.

Next, we define $P \in \mathbb{P}$ as an index for evaluating the time evolution of a flow field relative to that of the state space $\mathbb{J}$. The magnitude of the change in O is used to evaluate this and is determined by changes in both $\mathbb{J}$ within the set $\mathfrak{J}$ and the velocity field. In particular, we define $P = p(O_1, O_2)$, where $O_1 = o(\mathbb{J}_1)$, $O_2 = o(\mathbb{J}_2)$ for $\mathbb{J}_1, \mathbb{J}_2 \in \mathfrak{J}$. Here, $p(O_1, O_2)$ is a function defined on $\mathbb{O}$. Given this definition, P serves as a measure of the relationship between the state apace and flow field, and by determining O_1 and O_2 through the paths, it can be considered as a measure of time variation. Note, even if the time variation defined in this manner results in $P = p(o(\mathbb{J}_1), o(\mathbb{J}_2)) = 0$, it does not necessarily imply that $\mathbb{J}_1 = \mathbb{J}_2$.

From the perspective of dynamical systems, we consider the following. When the initial state space $\mathbb{J}_{t_0}$ evolves along the trajectory $\mathfrak{t} \subset \mathbb{T}_{\mathbb{U},r_0} \in \mathfrak{T}$ until time t_T, the resulting state space $\mathbb{J}_{\mathbb{SH}} \in \mathfrak{J}$ is given by $g_{\mathbb{SH}}(\mathbb{J}_{t_0})$. The state space $\mathbb{J}_{\mathbb{SH}}$ can be obtained from $\mathbb{J}_{t_0}$ using $\mathbb{U}, r_0, t_T$, but as we have discussed so far, from the viewpoint of limiting the analysis to infinitesimal regions, the quantities that correspond well to the time evolution of the state space are $\mathbb{SH}$ and $\mathbb{D}$. Therefore, the discussion proceeds primarily in $\mathbb{SH}$ and $\mathbb{D}$, especially in $\mathbb{D}$. However, $\mathfrak{t}$, which contains position information, is crucial and indispensable when considering spatial variations in the brightness of the visualization. Next, the quantities I, O, P projected from $\mathbb{J}_{\mathbb{SH}}$ are uniquely determined along $\mathbb{D}$. In particular, $\mathbb{O}, \mathbb{P}$ are the projections mapped along $\mathbb{D}$, which is different for each trajectory. There is no bijective mapping between $\mathfrak{S}\mathfrak{H}_{\mathbb{U}}$ and $\mathfrak{D}_{\mathbb{U}}$.

Therefore, we define $\mathbb{I}_{\mathbb{D}}, \mathbb{O}_{\mathbb{D}}, \mathbb{P}_{\mathbb{D}}$ ($\mathbb{I}_{\mathbb{D}} \subset \mathbb{I}, \mathbb{O}_{\mathbb{D}} \subset \mathbb{O}, \mathbb{P}_{\mathbb{D}} \subset \mathbb{P}$) corresponding to the velocity gradient trajectory $\mathbb{D} \in \mathfrak{D}_{\mathbb{U}}$. Then, the dynamics within the *velocity gradient history space*(*shear history space*) $\mathbb{A}_{\mathbb{D}} = \mathbb{I}_{\mathbb{D}} \times \mathbb{O}_{\mathbb{D}} \times \mathbb{P}_{\mathbb{D}}$ are constructed as follows:

$$\frac{dI}{dt} = A_I(I, O, P),$$
$$\frac{dO}{dt} = A_O(I, O, P),$$
$$\frac{dP}{dt} = A_P(I, O, P).$$

where A_I, A_O, A_P are the appropriate mappings defined on $\mathbb{A}_{\mathbb{D}}$. The defined space $\mathbb{A}_{\mathbb{D}}$ may contain attractors, periodic orbits, or a limit cycle. By observing the time evolution within $\mathbb{A}_{\mathbb{D}}$, it is evident that the flow's structure can be captured along a particular trajectory. The POD on the real-space trajectory, relationship between the POD and flow, and their time evolutions are represented. Furthermore, such dynamics are autonomous (not necessarily closed). As mentioned earlier, the space $\mathbb{A}_{\mathbb{D}}$ corresponds to the finite trajectory, and even if attractors or a limit cycle exist within $\mathbb{A}_{\mathbb{D}}$, it should be noted that a comprehensive understanding of the entire flow field is not possible.

In this study, we investigated the dynamics within $\mathbb{A}_{\mathbb{D}}$ for particles suspended in a time-dependent two-dimensional flow. According to Eq.(2), the orientation of the flaky particles suspended in a two-dimensional flow converges onto the flow plane. Therefore, $\mathfrak{J}$ is defined as the set of all state spaces $\mathbb{J}$ consisting of N points on the unit circumference. Moreover, we define the mapping i from $\mathfrak{J}$ to $\mathbb{I}_{\mathbb{D}}$ using each element $\boldsymbol{s}_n = (s_{n,x}, s_{n,y})$ of $\mathbb{J} \in \mathfrak{J}$ as follows:

$$i : \mathrm{tr}(\overleftrightarrow{T})^2 - 4\det(\overleftrightarrow{T}), \tag{4}$$

where the directional tensor, $\overleftrightarrow{T}$, introduced in Ref.[13)] is

$$\overleftrightarrow{T} = \frac{1}{|\mathbb{J}|} \sum_{\boldsymbol{s}_n \in \mathbb{J}} \overleftrightarrow{T}_n,$$

$$\overleftrightarrow{T}_n = \begin{pmatrix} s_{n,x}^2 & s_{n,x}s_{n,y} \\ s_{n,y}s_{n,x} & s_{n,y}^2 \end{pmatrix}.$$

When the distribution within the angle of inclination, $\phi \sim \phi + \Delta\phi$, is represented as $P(\phi)d\phi$ in $N \to \infty$, the value of i in Eq.(4) equals to $(\int_0^{2\pi} \cos 2\phi P(\phi)d\phi)^2 + (\int_0^{2\pi} \sin 2\phi P(\phi)d\phi)^2$. Taking into account that the expression of i is the coefficient of Fourier expansion, note that the minimum value of i is zero not only for the uniform distribution but also for any $P(\phi) = \frac{1}{2\pi} + \sum_{n=2}^{\infty} a_n \cos(2n\phi) + b_n \sin(2n\phi)$. In addition, under $\int_0^{2\pi} P(\phi)d\phi = 1$ and $P(\phi) > 0$, the maximum value of i is 1 for $P(\phi) = \delta(\phi - \phi_0)$ Thus, the degree of i describes anisotropy.

According to this definition, the state space $\mathbb{J} \in \mathfrak{I}_{unidirection}$ projected by i is mapped to 1, representing the POD anisotropy.

Moreover, we define the map $o_{\mathbb{D}}$ from $\mathfrak{I}$ to $\mathbb{O}_{\mathbb{D}}$ is defined as follows:

$$o_{\mathbb{D}} : \frac{1}{|\mathbb{J}|} \sum_{\boldsymbol{s}_n \in \mathbb{J}} |\boldsymbol{s}_n \cdot \boldsymbol{e}|, \tag{5}$$

in $\nabla \boldsymbol{u} \in \mathbb{D}$, where

$$(\nabla \boldsymbol{u} - \lambda \overleftrightarrow{I})\boldsymbol{e} = \boldsymbol{0}, \ \lambda \in \sigma(\nabla \boldsymbol{u}).$$

The set $\sigma(\nabla \boldsymbol{u}(t))$ represents the set of all eigenvalues of $\nabla \boldsymbol{u}(t)$, and $\boldsymbol{e}$ is the eigenvector corresponding to the eigenvalue λ. By selecting a single $\boldsymbol{e}$ at the initial position r_0 and ensuring that $\boldsymbol{e}$ varies smoothly along the trajectory, we obtain $\mathbb{O}_{\mathbb{D}}$, which has a time-smooth O. In a situation where the POD is isotropically distributed in $N \to \infty$, that is, when $i(\mathbb{J}) = 0$, we have $o_{\mathbb{D}}(\mathbb{J}) = 2/\pi$. The value of $\boldsymbol{e}$, which is required to calculate $o_{\mathbb{D}}$, contains the flow information which is principally unkown in visualization experiments, so that the value of $o_{\mathbb{D}}$ may be a clue for an experimenter to know the flow information.

Finally, we define the map $p_{\mathbb{D}}$ on $\mathbb{O}_{\mathbb{D}}$ as follows:

$$p_{\mathbb{D}} : \frac{o(g_{\mathbb{SH}_1}(\mathbb{J}_{t_0})) - o(g_{\mathbb{SH}_2}(\mathbb{J}_{t_0}))}{dt}, \tag{6}$$

$$\mathfrak{t}_1 = \{\boldsymbol{r}(t)|\, t \in [t_0, t_T]\}, \ \mathfrak{t}_2 = \{\boldsymbol{r}(t)|\, t \in [t_0, t_T - dt]\}.$$

where $\mathfrak{t}_1$ and $\mathfrak{t}_2$ provide $\mathbb{SH}_1$ and $\mathbb{SH}_2$, respectively. $\mathbb{J}_{t_0}$ is the state space at $\boldsymbol{r}_0 = \boldsymbol{r}(t_0)$ at time t_0, and $p_{\mathbb{D}}$ gives $P_{t_T} \in \mathbb{P}_{\mathbb{D}}$ and P at time t_T.

3. Results

In this study, we analyzed the shear history space $\mathbb{A}_{\mathbb{D}}$ for several examples of time-varying two-dimensional flows, where $\mathbb{D} \in \mathfrak{D}_{\mathbb{U}}$.

Let α be the inclination angle of $\boldsymbol{s}$ to x-axis, and let $\boldsymbol{e}_\alpha$ be defined as $\boldsymbol{e}_\alpha := -\sin\alpha \boldsymbol{e}_x + \cos\alpha \boldsymbol{e}_y$. Additionally, let $\lambda(t)$ be one of the two eigenvalues of the time-dependent symmetric velocity gradient tensor, and let the corresponding eigenvector be expressed as $\boldsymbol{e} := \cos\phi(t)\boldsymbol{e}_x + \sin\phi(t)\boldsymbol{e}_y$. Then,

$$\nabla \boldsymbol{u} \quad = \quad \begin{pmatrix} \cos\phi(t) & -\sin\phi(t) \\ \sin\phi(t) & \cos\phi(t) \end{pmatrix} \begin{pmatrix} \lambda(t) & 0 \\ 0 & -\lambda(t) \end{pmatrix} \begin{pmatrix} \cos\phi(t) & \sin\phi(t) \\ -\sin\phi(t) & \cos\phi(t) \end{pmatrix},$$

determine the time evolution of $\boldsymbol{s}$, based on $\frac{d\boldsymbol{s}}{dt} = \frac{d\alpha}{dt}\boldsymbol{e}_\alpha$ and $\boldsymbol{s} \times \boldsymbol{s} \times (\nabla \boldsymbol{u} \cdot \boldsymbol{s}) = -\boldsymbol{e}_\alpha(\boldsymbol{e}_\alpha \cdot \nabla \boldsymbol{u} \cdot \boldsymbol{s})$.

From these and Eq.(2), we obtain

$$\frac{d\alpha}{dt} = \lambda(t)\sin\left(2(\alpha - \phi(t))\right). \tag{7}$$

This leads to the conclusion that, corresponding to the negative eigenvalue, the POD will converge along the direction of the eigenvector at a time scale determined by the eigenvalue, as derived from Eq.(2).

We studied three functional forms with respect to $\lambda(t)$ and $\phi(t)$. Specifically, $N = 50,000$ orientations were initialized at time $t_0 = 0$ such that $i(\mathbb{J}_0) = 0$ by dividing the circumference into N equivalents, and numerical simulations were performed using the fourth order Runge–Kutta method (with a time step of $\Delta t = 10^{-4}$) in the absence of an analytical solution. The time series of I, O, and P differ depending on the initial state $\mathbb{J}_0$. However, this study mostly focuses on the case in which the initial distribution of orientations is isotropic.

As the flakey particles drift within the flow, the attracting eigenvector between the two orthogonal eigenvectors may switch. For example, consider the case where the direction of the eigenvectors of $\nabla\boldsymbol{u} \in \mathbb{D}$ remains constant, whereas the sign of $\lambda(t)$ alternates periodically.

(i) $\lambda(t) = \cos(\omega t), \phi(t) = 0$

$$\frac{d\alpha}{dt} = \cos(\omega t)\sin(2\alpha). \tag{8}$$

where the analytical solution for α is $\alpha = \tan^{-1}(e^{\frac{2}{\omega}\sin\omega t}\tan\alpha(0))$.

Let the shear history space obtained in (i) be denoted as $\mathbb{A}_{\mathbb{D}_\omega}$. FIG.2 illustrates the trajectories of I, O, P within $\mathbb{A}_{\mathbb{D}_\omega}$. The figure shows the trajectories for $\omega = \pi/10, 3\pi/10, 6\pi/10, \pi$, indicating that isotropization and anisotropization occur periodically. If the periods of I, O, P are denoted as T_I, T_O, T_P, respectively, they satisfy $2T_I = T_O = T_P = 2\pi/\omega$. Furthermore, the values of P are symmetric with respect to the I–O plane at $P = 0$. As ω increases, the degree of anisotropization weakens, indicating that the attracting eigenvector switches rapidly. For $\omega = 0$, irrespective of its initial value, α converges to $\alpha = \pi/2$, which leads to $I = 1$. In the limit $\omega \to \infty$, $I = 0$, $O = 2/\pi$, and $P = 0$ remain unchanged from their initial values. Thus far, this discussion has been based on the initial condition $I = 0$, whereas FIG.3 presents trajectories for different initial conditions within $\mathbb{A}_{\mathbb{D}_{3\pi/10}}$ (i.e., for $\omega = 3\pi/10$). The properties described above hold regardless of the initial conditions, suggesting the existence of an infinite number of periodic orbits. From the trajectories in $\mathbb{A}_{\mathbb{D}_\omega}$, it follows that if the shear history obtained in (i) is applied to the particles, the periodicity in the flow can be inferred from the experimental visualization. Moreover, it is expected that the periodicity of misalignment between the direction of the eigenvector and the particle orientation can be measured

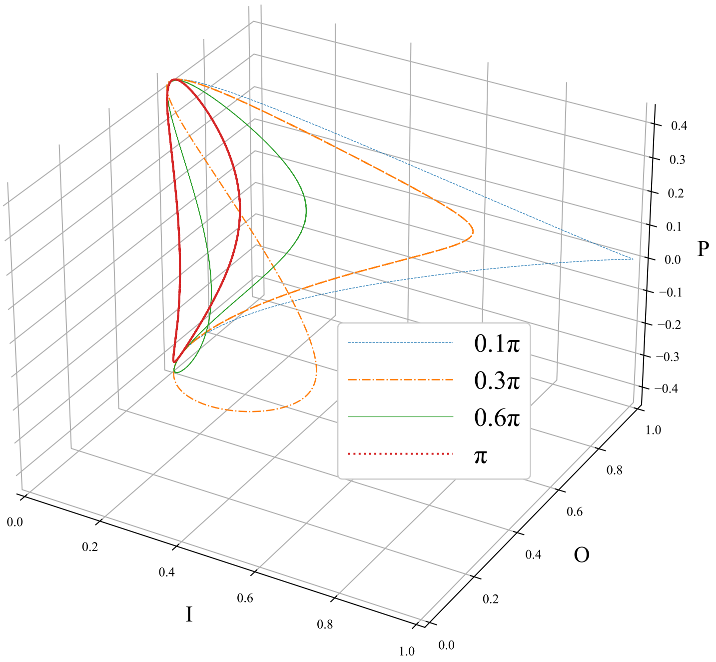

Fig. 2. Time evolution of I, O, and P in $\mathbb{A}_{\mathbb{D}_\omega}$. For $\omega = \pi/10, 3\pi/10, 6\pi/10, \pi$, the periods satisfy $T_O = T_P = 2T_I$. I and O reach their maximum values simultaneously.

experimentally, which will be discussed in detail in the next section.

Let us incorporate the effects of the two orthogonal eigenvectors of the velocity gradient tensor rotating at a constant angular velocity over time into the previously discussed model. The direction of the eigenvector, denoted by $\phi(t)$, is time-evolved linearly as follows:

(ii) $\lambda(t) = \cos(\omega_1 t), \phi(t) = \omega_2 t$

$$\frac{d\alpha}{dt} = \cos(\omega_1 t)\sin(2(\alpha - \omega_2 t)). \tag{9}$$

The time evolutions within the shear history space $\mathbb{A}_{\mathbb{D}_{\omega_1,\omega_2}}$ were investigated at the lattice points on $n\pi$ $(n = 0, 1, \ldots, 10)$ for ω_1, ω_2. Several characteristic orbits were observed in the phase-space diagram for ω_1, ω_2 (FIG.4). Whether the POD aligns with the direction of the flow ’ s eigenvectors depends on the values of ω_1 and ω_2.

First, when $\omega_1 = \omega_2 = 0$, that is, $\alpha = \tan^{-1}(e^{2t}\tan\alpha(0))$, the system converges to the

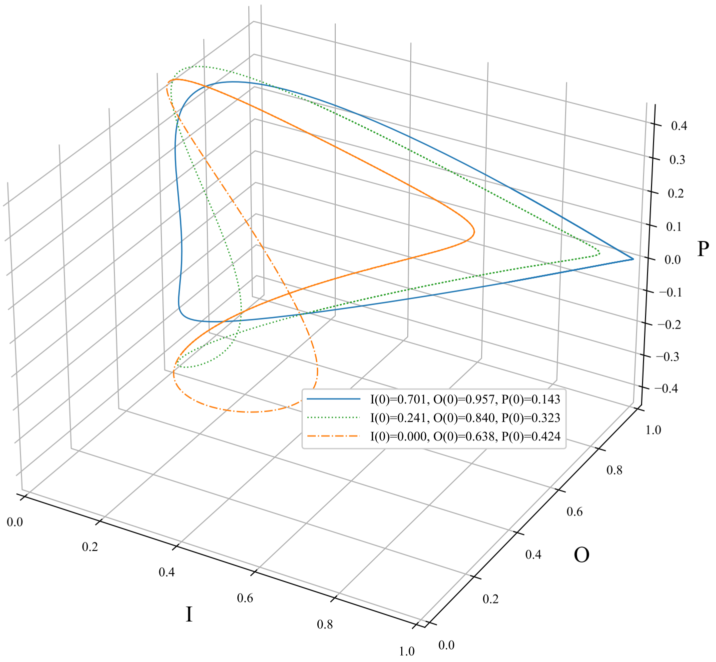

Fig. 3. Time evolution of I, O, and P in the $\mathbb{A}_{\mathbb{D}_{3\pi/10}}$. The plots are shown for $(I(0), O(0)) = (0.701, 0.957), (0.241, 0.840), (0.000, 0.638)$. I and O reach their maximum values simultaneously.

attractor $(I, O, P) = (1, 1, 0)$. This corresponds to a flow in which the velocity field to which the particles are exposed does not change, and the shear of the flow can be obtained through visualization. The plane Couette flow differs from that in Eq.(9) because it possesses vorticity; however, it is equivalent in the sense that the attracting eigenvector does not change over time. A plane Couette flow contains an attractor within $\mathbb{A}_{\mathbb{D}}$ for $\mathbb{D} \in \mathfrak{D}_{couette}$. Next, for $\omega_1 = 0$ and $\omega_2 \neq 0$, an elliptical periodic orbit is formed, as shown in FIG.4B. Here, $T_I = T_O = T_P$, and the phase shift can be confirmed between each of these systems. The periodicity of the flow can be inferred from the changes in brightness obtained through visualization. Furthermore, it can be observed from Eq.(9) that a bifurcation occurs at $\omega_2 = 1$. As shown in FIG.5, an attractor is formed for $\omega_2 \leq 1$. However, when $\omega_1 \neq 0$ and $\omega_2 = 0$, the time evolutions can be described by Eq.(2) and are shown in FIG.4C. When $\omega_2/\omega_1 = 1/2$, a limit cycle is formed in the $O - P$ plane for sufficiently long paths t, where $I = 1$ (FIG. 4D). Finally,

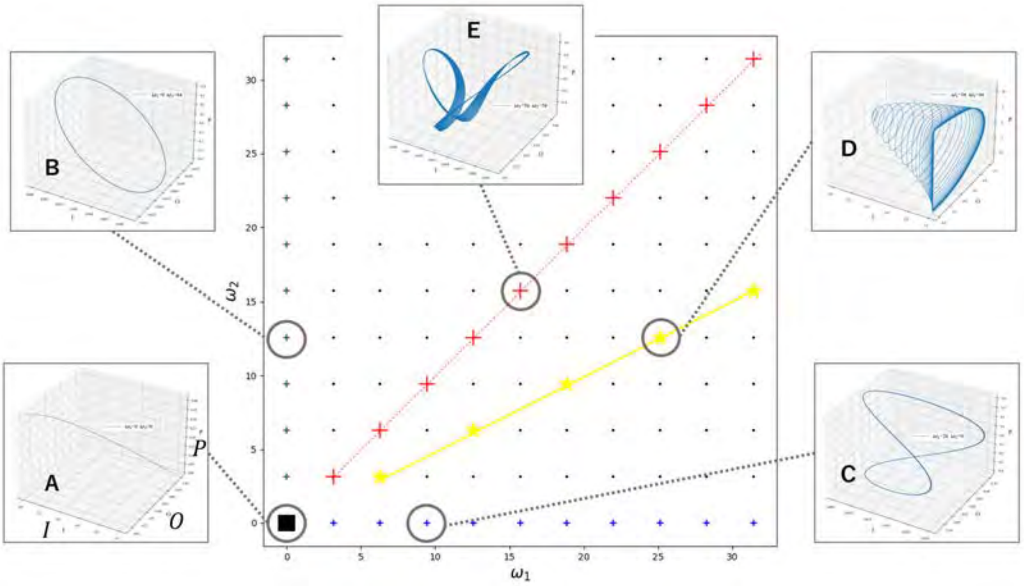

Fig. 4. Phase space diagram of ω_1, ω_2 in the dynamical system within $\mathbb{A}_{\mathbb{D}_{\omega_1,\omega_2}}$. For $\omega_1 = \omega_2 = 0$, an attractor is formed. For $\omega_1 = 0, \omega_2 \neq 0$, elliptical orbits appear, and bifurcations occur at $\omega_2 = 1$ and behave similar to those shown in FIG.5. For $\omega_1 \neq 0, \omega_2 = 0$, orbits identical to those in Eq.(8) are observed. Additionally, a limit cycle exists when $\omega_2/\omega_1 = 1$, and characteristic orbits are formed when $\omega_2/\omega_1 = 1/2$.

for $\omega_2/\omega_1 = 1$, the orbits shown in FIG.4E (FIG.6) are observed. As ω_1 is increased while maintaining $\omega_1 = \omega_2$, The narrowing of the width of the alternating periodic orbits that make up a single orbit suggests that the orbit is approaching a perfect periodic orbit with ω_1 and ω_2 at infinity.

Finally, we oscillate $\phi(t)$.

(iii) $\lambda(t) = \cos(\omega_1 t), \phi(t) = A\cos(\omega_2 t)$

$$\frac{d\alpha}{dt} = \cos(\omega_1 t)\sin(2(\alpha - A\cos(\omega_2 t))). \tag{10}$$

Three nondimensional parameters, ω_1, ω_2, and A, exist, and, as in Eq.(8) and Eq.(9), attractors and periodic orbits are observed. Additionally, more diverse complex trajectories, which did not occur as a result of the previous two equations, are confirmed (FIG.7). A variety of trajectories can be seen in $\mathbb{A}_{\mathbb{D}_{\omega_1,\omega_2,A}}$, which is obtained in (iii). Some examples of these trajectories are provided and their characteristics are listed. FIGS.7A and C illustrate the trajectories that are expected to converge to $I = 1$. FIG.7B shows a trajectory resembling a superposition of those in $\mathbb{A}_{\mathbb{D}_\omega}$(FIG.2). FIG.7D presents a distinctive trajectory in which an additional tubular structure exists within a larger tubular orbit. In FIG.7E, the trajectory converges within the $I = 1$ plane, where a smaller circular orbit is embedded within a larger

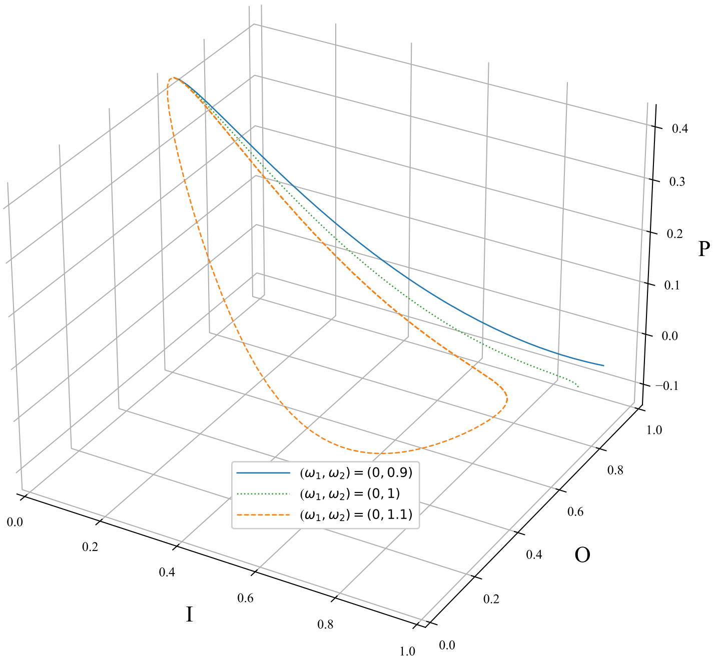

Fig. 5. Time evolutions of I, O, and P in $\mathbb{A}_{\mathbb{D}_{0,\omega_2}}$ for $\omega_2 = 1.1, 1, 0.9$.

one. Finally, FIG.7F shows a complex trajectory with no apparent regularity.

The information obtained from the flow-visualization experiments based on the trajectories within $\mathbb{A}_{\mathbb{D}}$ for (i), (ii), and (iii), as described previously, is discussed in the following section.

4. Discussion

4.1 Limitation of interpretation from visualization

In Section 3, the relationship between flow and state space $\mathbb{J}$ was mapped onto the shear history space $\mathbb{A}$, and the time evolution of I, O, P within $\mathbb{A}$ were observed. In this section, we focus on I and O, which constitute $\mathbb{A}$, and conduct an analysis from an optical perspective.

In optical visualization using flaky particles, we assume that the only information obtainable by the experimenter is the brightness reflected by the particles. The relationship between brightness and $\mathbb{J}$ can be considered as follows.

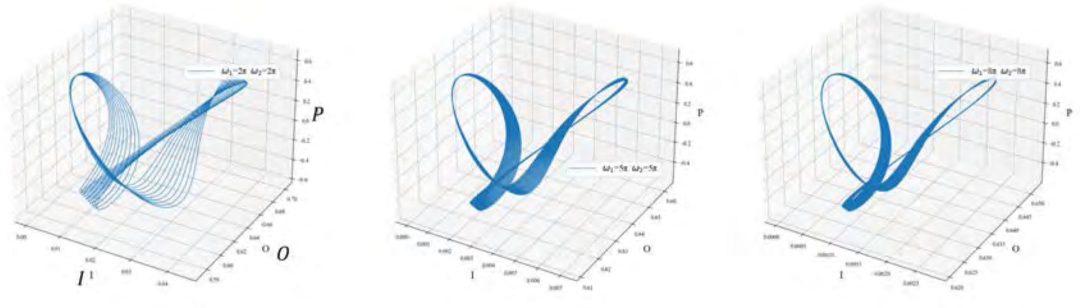

Fig. 6. Time evolutions of I, O, P for $\omega_1 = \omega_2$. From left to right, $(\omega_1, \omega_2) = (2\pi, 2\pi), (5\pi, 5\pi), (8\pi, 8\pi)$. $(5\pi, 5\pi)$ corresponds to Fig. 4 E. As $\omega_1 = \omega_2$ increases, the width of the repeated trajectory narrows.

From the perspective of visualization experiments, let the optical axis vector of the camera be denoted as $\boldsymbol{C}$ and the incident light vector from the light source as $\boldsymbol{I}$. Furthermore, let β be the angle between the bisector of these two vectors and $\boldsymbol{I}$, and let the corresponding vector be denoted as $\boldsymbol{R}$. Based on these, the intensity of the reflected light captured by the camera, B, is expressed by the following equation.

$$B = \frac{1}{|\mathbb{J}|} \sum_{\boldsymbol{s}_n \in \mathbb{J}} |\boldsymbol{s}_n \cdot \boldsymbol{R}|.$$

In visualization experiments, the only directly measurable quantity for the experimenter is the brightness B. Therefore, this study examines whether information about the flow field can be extracted from variations in B. In particular, we investigate whether the periodicity and direction of shear—specifically, the eigenvector $\boldsymbol{e}$ of the velocity gradient tensor—can be estimated. If the brightness exhibits periodic variations, it can be inferred that the shear periodicity is identifiable; however, this does not necessarily imply that the shear direction can be determined.

The following section describes the conjecture an experimenter would likely make to obtain $\boldsymbol{e}$ from visualization. Subsequently, the estimation results of $\boldsymbol{e}$ based on these conjectures are presented, followed by a discussion of their validity.

4.1.1 Conjecture and Estimation from the Experimenter's Perspective

In this section, we consider the Conjectures an experimenter might make when relying solely on brightness information in visualization experiments. Under such conditions, the only viable analytical approach for the experimenter is to connect brightness and flow field

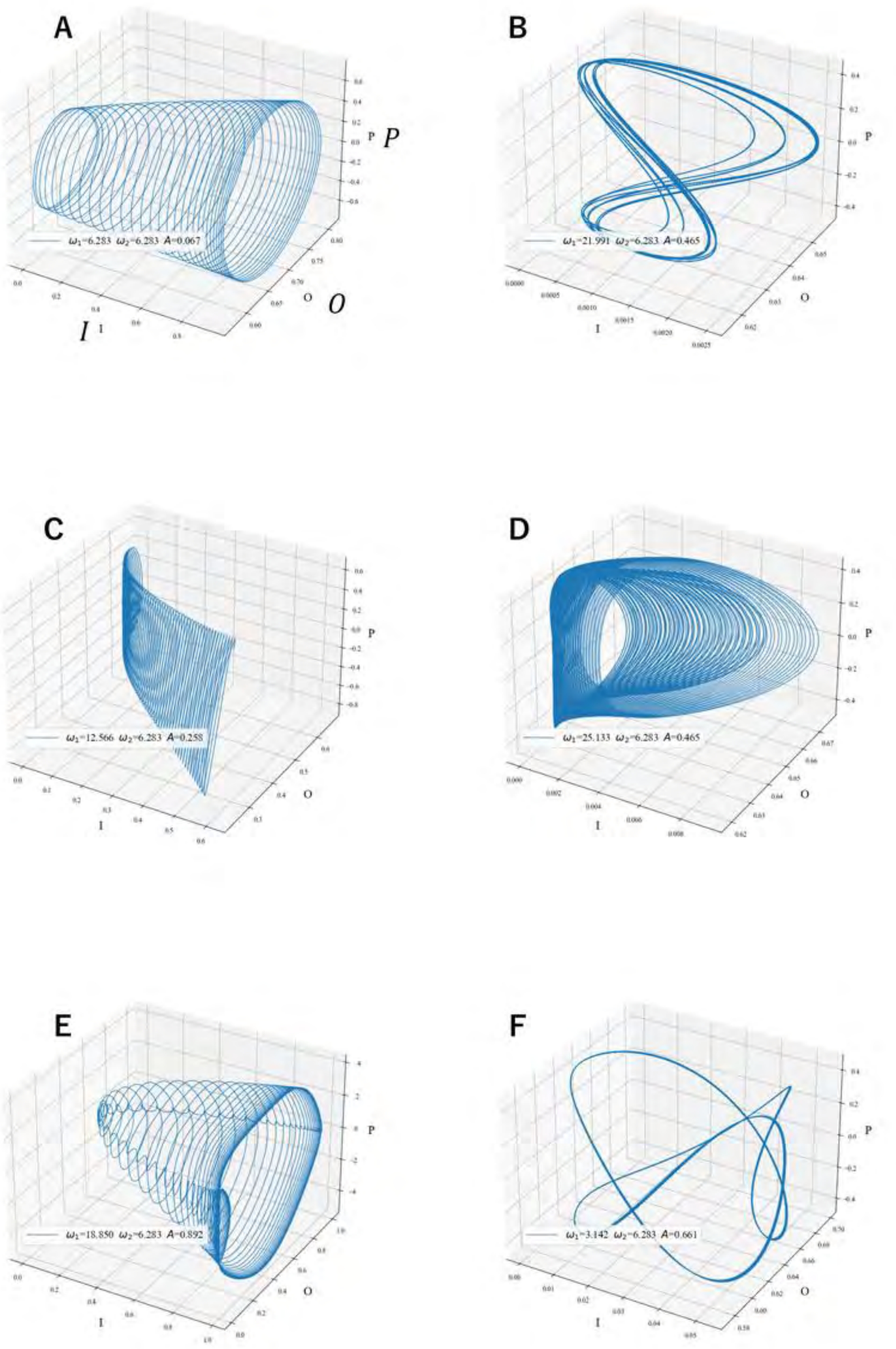

Fig. 7. Time evolution of various trajectories for I, O, P at $\omega_2 = 2\pi$. Top row, from left: $(\omega_1, A) = (2\pi, 0.067), (7\pi, 0.465), (4\pi, 0.258)$. Bottom row, from left: $(\omega_1, A) = (8\pi, 0.465), (6\pi, 0.892), (\pi, 0.661)$.

information. Since brightness depends on the state space $\mathbb{J}$ and POD, and $\mathbb{J}$ is generated by $\mathbb{D}$, the following conjecture can be drawn:

”Predict POD from brightness B and estimate the eigenvector $\boldsymbol{e}$ of the velocity gradient tensor.”

To assess whether this approach can serve as a valid method for the experimenter, we offer a more constrained perspective and develop reasoning based on specific assumptions.

$*1$ Experimenter’s Conjecture

”POD converges in the direction of the eigenvector $\boldsymbol{e}$” $\Leftrightarrow O = 1, I = 1$

Based on this assumption, the experimenter interprets the temporal variations in brightness as corresponding to the temporal variations in the converged orientations. Furthermore, given that the POD is converging in the direction of $\boldsymbol{e}$, the following logical step emerges:

”The temporal variation of brightness B corresponds to the rotation of $\boldsymbol{e}$.”

$*2$ Experimenter’s Estimation

”For a time-varying B , when B is maximized, $\boldsymbol{e}$ is parallel to $\boldsymbol{R}$, and when B is minimized, $\boldsymbol{e}$ is perpendicular to $\boldsymbol{R}$.”

Based on the assumptions $*1$ and $*2$, the experimenter estimates $\boldsymbol{e}$. In this study, we analyze three different brightness variation situations, as shown in FIG. 8, and discuss the accuracy of eigenvector estimation in each case.

4.1.2 Estimation from the Experimenter’s Perspective

In the following, we present estimation based on assumptions $*1$ and $*2$ for three situations of temporal brightness variation (FIG. 9). Let $\boldsymbol{e}^*$ denote the eigenvector estimated by the experimenter, and ϕ^* the angle between $\boldsymbol{e}^*$ and $\boldsymbol{R}$.

Situation 1: No Change in Brightness (FIG. 8, Left) The brightness measured by the experimenter remains constant B_{const}. In this case, the maximum and minimum observed brightness is $B_{\max} = B_{\min} = B_{\text{const}}$, and according to assumption $*2$, the eigenvector is always estimated to be parallel to $\boldsymbol{R}$, yielding $\phi^* = 0$. Consequently, the experimenter ’ s estimation is illustrated in FIG. 9 (Left, Situation 1).

Situation 2: Brightness Varies Without Reaching Zero (FIG. 8, Center) The estimated eigenvector direction does not pass through the direction perpendicular to $\boldsymbol{R}$ (denoted as $\boldsymbol{R}_{\perp}$), as illustrated in FIG. 9 (Center, Situation 2). According to assumption $*1$, as brightness

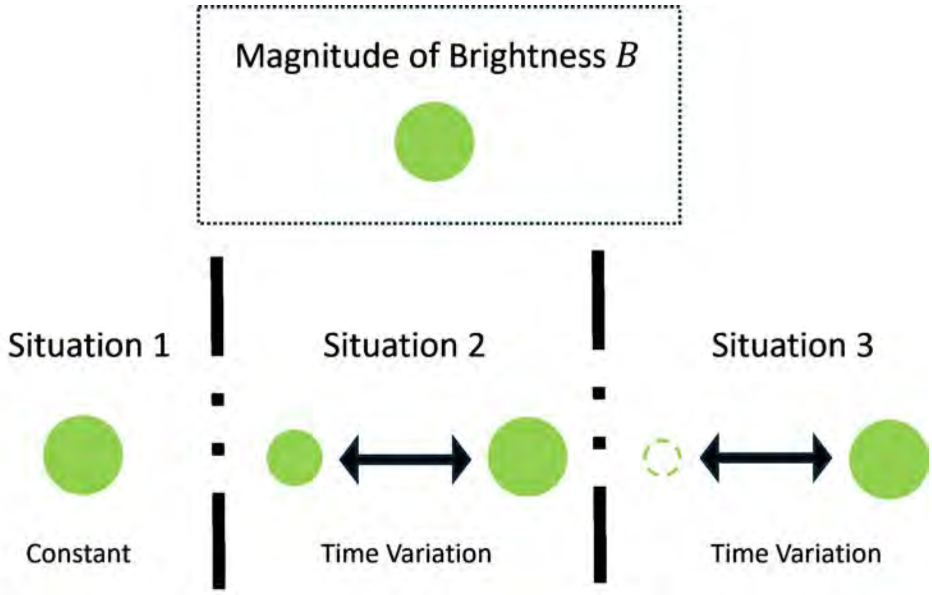

Fig. 8. Situations of time variation in the brightness B measured by the experimenter. The left shows a case where the brightness remains unchanged. The center and right show cases where the brightness varies over time. In particular, in the right case, there are moments when the brightness becomes zero during the time variation.

decreases, $\boldsymbol{e}^*$ monotonically leaves from $\boldsymbol{R}$. Assumption $*2$ dictates that when brightness is maximized, $\phi^* = 0$, and when brightness is minimized, $\phi^* = \pi/2$.

Situation 3: Brightness Varies and Reaches Zero (FIG. 8, Right) The eigenvector is estimated to pass through $\boldsymbol{R}_\perp$, as depicted in FIG. 9 (Right, Situation 3). Similar to Situation 2, $\boldsymbol{e}^*$ monotonically leaves from $\boldsymbol{R}$ as brightness decreases. Assumption $*2$ ensures that when brightness is maximized, $\phi^* = 0$, and when brightness is minimized, $\phi^* = \pi/2$.

4.1.3 Validity of Estimation

In the following, we verify the validity of the estimation (FIG. 9) under assumptions $*1$ and $*2$ for three situations of brightness variation. We first consider cases where assumption $*1$ holds, followed by an analysis of several trajectories within the shear history space $\mathbb{A}$ presented in Section 3 of this paper.

First, we examine the three scenarios where assumption $*1$ holds, meaning that $I = O = 1$. Since $O = 1$, the all normal vectors in POD are aligned with $\boldsymbol{e}$. Let ϕ denote the angle between $\boldsymbol{e}$ and $\boldsymbol{R}$.

(1) Case where the eigenvector $\boldsymbol{e}$ does not change direction (FIG. 10, Left)

In this scenario, the brightness remains constant. Consequently, the experimenter estimates $\boldsymbol{e}^*$ as shown in FIG. 9 (Situation 1), leading to $\phi^* = 0$ and an estimation error of

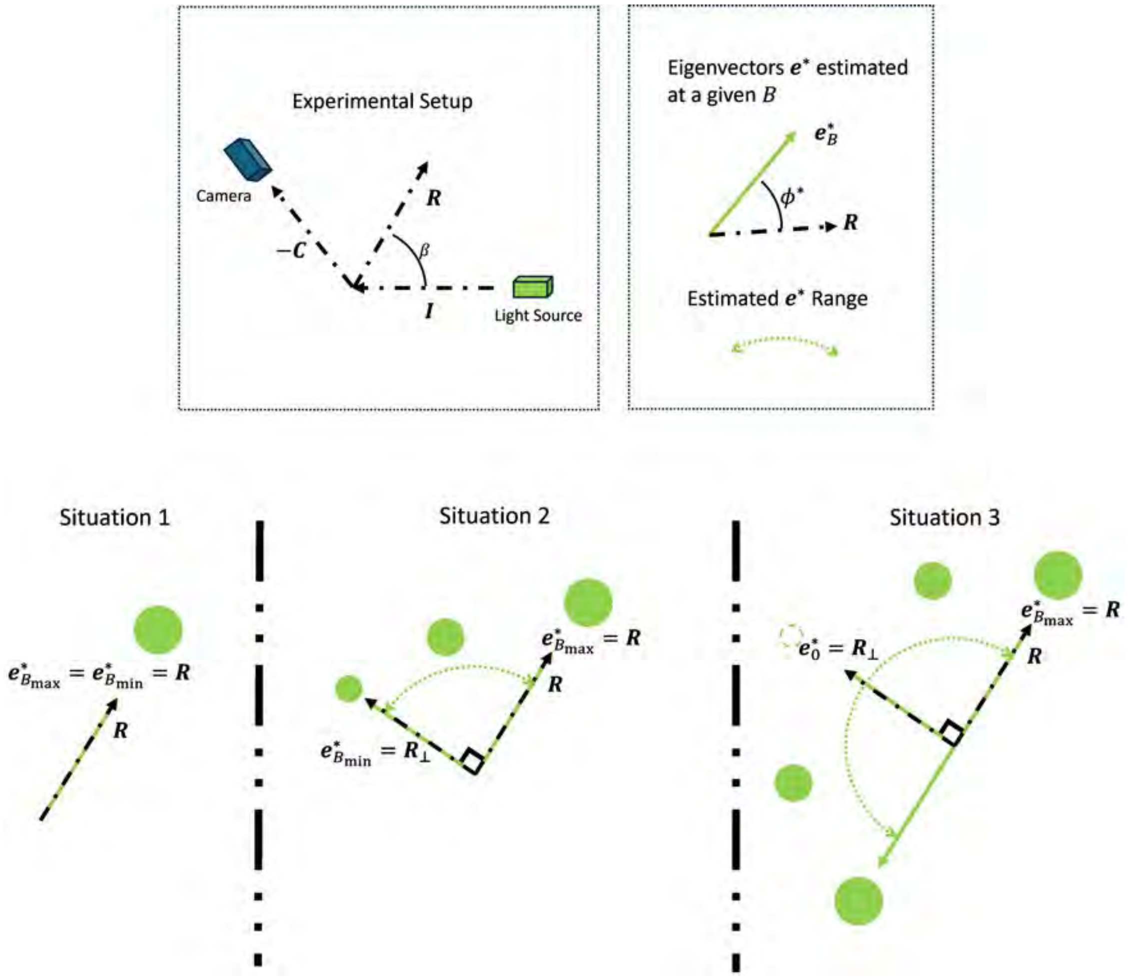

Fig. 9. Situations of time variation in the brightness B measured by the experimenter and the estimation of the eigenvector $\boldsymbol{e}^*$. The left case represents a scenario where the brightness remains unchanged, leading the experimenter to estimate that the eigenvector $\boldsymbol{e}$ does not change over time. The center and right cases correspond to scenarios where the brightness varies. In the center case, the estimated eigenvector does not pass through $\boldsymbol{R}_\perp$, whereas in the right case, it does.

$|\phi - \phi^*|$, which does not change over time (FIG. 11A). FIG. 11 illustrates the relationship between brightness B and the eigenvector (both actual $\boldsymbol{e}$ and estimated $\boldsymbol{e}^*$). The solid black line f represents the actual relationship between $\boldsymbol{e}$ and B, and is a monotonic function defined for $0 < \phi < \pi/2$. (For $\pi/2 < \tilde{\phi} < \pi$, a symmetric function $\tilde{f}$ exists such that $f(\phi) = \tilde{f}(\pi - \phi)$, making it impossible to distinguish ϕ from $\tilde{\phi}$ based on brightness alone.) Such a case corresponds to parallel shear flows like a plane Couette flow. Furthermore, by adjusting the camera position to capture maximum brightness, it may be possible to achieve $|\phi - \phi^*| = 0$.

(2) Case where the eigenvector $\boldsymbol{e}$ varies between $\boldsymbol{R}$ and $\boldsymbol{R}_\perp$ (FIG. 10, Center)

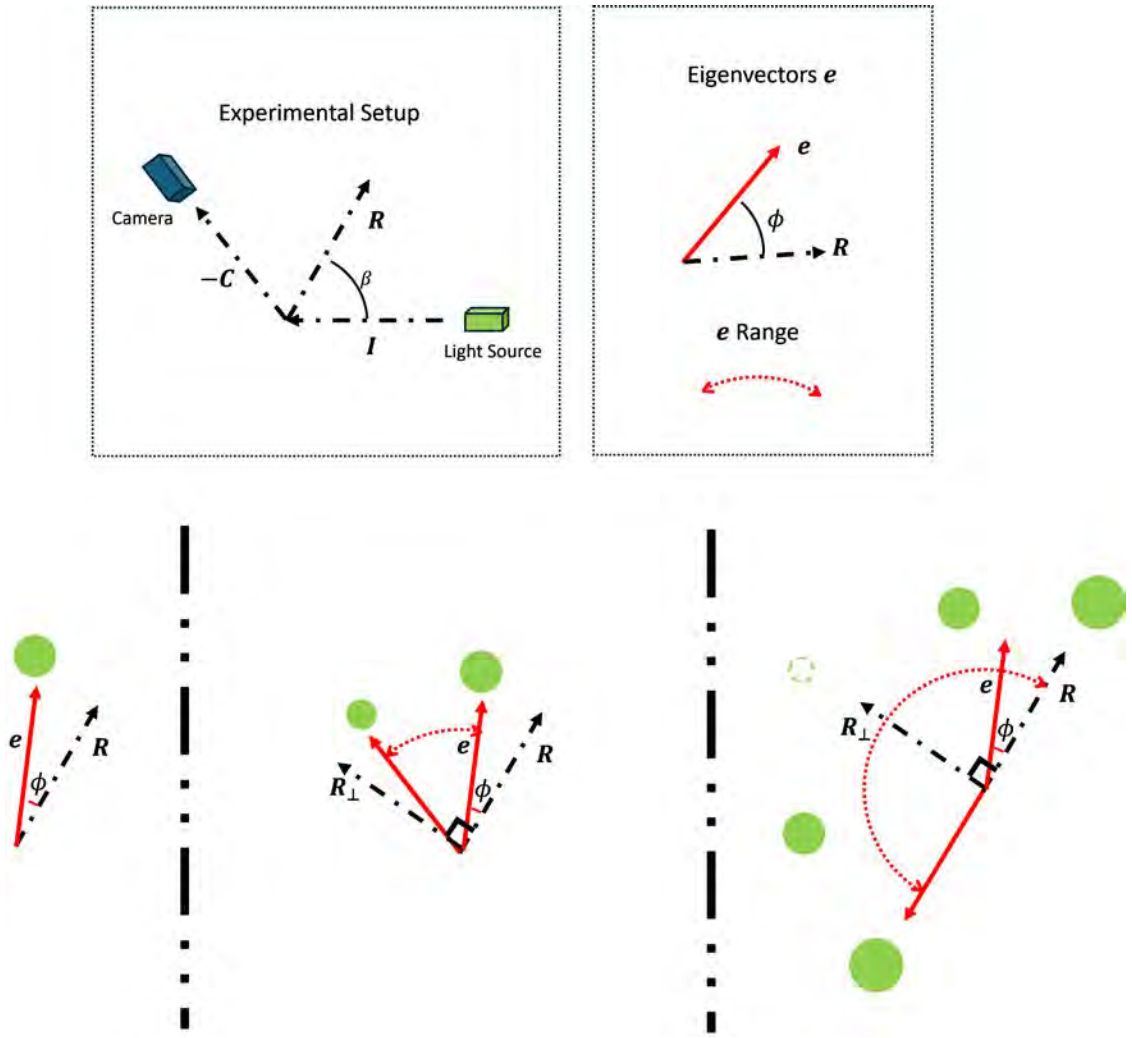

Fig. 10. Relationship between the actual eigenvector $\boldsymbol{e}$ and brightness B when $I = O = 1$. On the left, $\boldsymbol{e}$ does not change, and the brightness remains constant (the brightness varitation corresponds to Situation 1 in FIG.8). In the center, $\boldsymbol{e}$ varies between $\boldsymbol{R}$ and $\boldsymbol{R}_{\perp}$ over time, causing the brightness to vary (the brightness varitation corresponds to Situation 2 in FIG.8). On the right, $\boldsymbol{e}$ completes a full rotation, with the brightness taking a value of 0 while varing over time (the brightness varitation corresponds to Situation 3 in FIG.8).

In this scenario, the experimenter always measures positive brightness values and estimates ϕ^* as shown in FIG. 9 (Situation 2). As a result, there exists one brightness value $\hat{B}$ at which the estimated and actual values coincide, as shown in FIG. 11B. The dashed black line $g(B)$ represents the estimated ϕ^* obtained under assumptions $*1$ and $*2$, and is a monotonic function similar to f, defined for $0 < \phi^* < \pi/2$. (For $\pi/2 < \tilde{\phi}^* < \pi$, a symmetric function $\tilde{g}$ exists such that $g(\phi^*) = \tilde{g}(\pi - \phi^*)$, meaning the experimenter must consider both g and $\tilde{g}$.) Consequently, at the brightness $\hat{B}$ (blue point in FIG. 11B), the estimation is accurate ($f(\hat{B}) = g(\hat{B})$), while the estimation error $|\phi - \phi^*|$ increases as

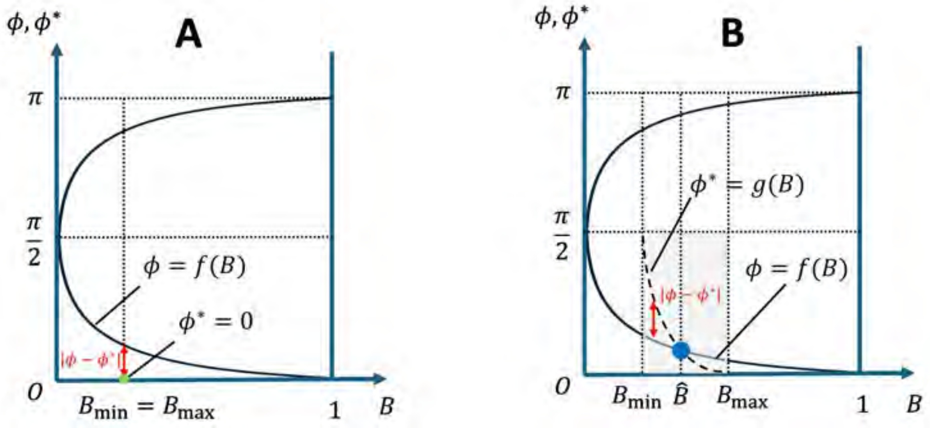

Fig. 11. The relationship between the estimated eigenvector $\boldsymbol{e}^*$ obtained from the brightness B measured by the experimenter and the actual eigenvector $\boldsymbol{e}$. When hypothesis $*1$ holds, the relationship between brightness and ϕ is given by a monotonic function f, defined in the range $0 < \phi < \pi/2$ (solid black line). Since the experimenter assumes hypothesis $*1$, they also estimate $\boldsymbol{e}^*$ using another monotonic function, expressed as $\phi^* = g(B)$ (dashed black line). For $\pi/2 < \tilde{\phi}, \tilde{\phi}^* < \pi$, symmetric functions $\tilde{f}$ and $\tilde{g}$ exist, satisfying $f(\phi) = \tilde{f}(\pi - \phi)$ and $g(\phi^*) = \tilde{g}(\pi - \phi^*)$, meaning that the experimenter considers both g and $\tilde{g}$. Additionally, the function satisfies $g(B_{\max}) = 0$ and $g(B_{\min}) = \pi/2$, where $B_{\max}$ and $B_{\min}$ are the maximum and minimum brightness values measured by the experimenter.

Case A represents the estimation error when the brightness remains unchanged, where $|\phi - \phi^*|$ does not vary over time. Case B corresponds to a scenario where the actual eigenvector moves between $\boldsymbol{R}$ and $\boldsymbol{R}_\perp$, resulting in a single brightness value $\hat{B}$ where the estimated and actual values coincide. As the brightness changes from $\hat{B}$, $|\phi - \phi^*|$ increases.

brightness leaves from $\hat{B}$.

(3) Case where the eigenvector $\boldsymbol{e}$ completes a full rotation (FIG. 10, Right)

Here, there exist moments when the measured brightness is $B = 0$. The experimenter estimates ϕ^* as shown in FIG. 9 (Situation 3), leading to agreement between the estimated and actual values at maximum and minimum brightness points (where $B_{\max} = 1$ and $B_{\min} = 0$). This scenario represents a case where brightness reaches $B = 0$, confirming that $\phi = \phi^* = \pi/2$ at minimum brightness from the experimenter's perspective. However, if $\boldsymbol{e}$ does not pass through $\boldsymbol{R}$, then at maximum brightness, $|\phi - \phi^*| \neq 0$, resembling the location relationship illustrated in FIG. 11B. It is important to note that the experimenter cannot find whether $\boldsymbol{e}$ has passed through $\boldsymbol{R}$.

Even when the relationship between the flow and the state space $\mathbb{J}$ converges to $I = O = 1$ within $\mathbb{A}$ (i.e., hypothesis $*1$ holds), the shear direction (i.e., the eigenvector $\boldsymbol{e}$ of the velocity gradient tensor) cannot be fully determined through optical visualization.

The following discussion examines $\mathbb{A}$ cases introduced in Section 3:

- FIG.4A represents a case where hypothesis $*1$ holds, and $I = O = 1$ converges. In this scenario, the eigenvector remains unchanged, corresponding to the left side of FIG.10.
- The green dashed line in FIG.5 represents a case where $I = 1, O = \hat{O} < 1$ converge. Here, the eigenvector $\boldsymbol{e}$ and the orientation $\hat{s}$ obtained via convergence of POD. In Eq.(9), this case corresponds to a situation where $\omega_2 \neq 0$, indicating that the eigenvector undergoes full rotation. Consequently, an experimenter assuming hypotheses $*1$ and $*2$ would make an estimation corresponding to Situation 3. The brightness B is determined by $\hat{s}$, resembling the situation depicted on the right side of FIG.10. This suggests that an additional error, which is approximately negatively correlated with $\hat{O}$, contributes to the error $|\phi - \phi^*|$ in case (3) of the previous section.
- In FIG.4D, $I = 1$ while O does not converge. In this case, the additional error associated with $|\phi - \phi^*|$ in case (3) of the previous section fluctuates with the temporal variation of O.
- In FIG.4C, neither I nor O converges, the experimenter's assumption $*1$ entirely misdirected. In this scenario, the measured brightness B exhibits periodic variation without approaching zero, leading the observer to estimate $\boldsymbol{e}^*$ as depicted in the central panel of FIG.9 (Situation 2). Although this assumption is incorrect, since the eigenvector remains unchanged such as $\omega_2 = 0$ in Eq.(9), the resulting error $|\phi - \phi^*|$ increases as the estimated value leaves from the actual value, as illustrated in FIG.11B (where $\phi = f(B) = \text{const}$).
- In FIG.4B, estimation corresponds to Situation 2 in FIG.9, but only periodic variations in brightness are observed, providing no meaningful information regarding the eigenvector direction.

In summary, when an experimenter attempts to infer the eigenvector $\boldsymbol{e}$ based on hypotheses $*1$ and $*2$, the shear direction can only be fully determined if hypothesis $*1$ holds rigorously and $\boldsymbol{e}$ remains unchanged, as seen in FIG.11A. When $\boldsymbol{e}$ varies over time, a monotonic relationship is obtained between $|\phi - \phi^*|$ and B, with errors reducing to zero when $\boldsymbol{e}$ passes through specific points (e.g., $\boldsymbol{R}$ and $\boldsymbol{R}_\perp$). If $I = 1$ converges but O does not, additional errors correlated negatively with O contribute to $|\phi - \phi^*|$ in case (3) of the previous section.

The shear history space $\mathbb{A}$ also serves as a framework for clarifying the conditions under which optical visualization provides meaningful information. According to this framework, optical visualization would be applicable only to FIG.7A in the flows considered in this study, excluding the cases discussed in Section 4-1.

In general, even if the flow field is periodic, the patterns obtained through visualization using flakey particles are not necessarily periodic. In such cases, the available flow information cannot be extracted. This is also true for steady flows, where the shear (velocity gradient tensor) to which the particles are exposed changes over time. Thus, the flow fields for which visualizations using POD characteristics are effective to extract $\boldsymbol{\nabla u}$ are limited. Furthermore, in actual visualization experiments, the time evolution within $\mathbb{A}_{\mathbb{D}}$, which we have analyzed thus far, is combined in a three-dimensional real space, resulting in light and dark patterns.

4.2 Neural Network Modeling

In the Section 4-2, the statistical properties of the orientation of flakey particles, denoted by I, O, and P, and their relationships with the flow field were observed. The relationship between the orientation and flow is closely related to the information obtained from experimental fluid visualization. Specifically, the dynamics of I, O, and P within $\mathbb{A}_{\mathbb{D}}$ were considered.

In recent years, machine-learning methods have been extensively studied and investigated for application in dynamical systems. In particular, chaotic behavior,[14] which is a characteristic of the dynamics and is also related to the dynamics within the shear history space $\mathbb{A}_{\mathbb{D}}$, appears in various fields such as geophysics,[15] robotics,[16] the power industry, and energy-related problems, and fluid dynamics[17, 18] is no exception.

Regarding neural network models for dynamical systems, models such as long short-term memory (LSTM), which are widely used for learning time-series data in fields such as natural language processing, are well known. In recent years, various approaches to time-series data,[19] including dynamical system deep learning (DSDL),[20] have been developed and actively compared.[21] Moreover, predictions of time evolution using these models have already been applied in the aforementioned fields, where accurate and long-term predictions remain challenging. As a result, since the 1990s, various machine-learning models for handling time-series data have been proposed.[22, 23]

This study does not aim to develop a long-term, highly accurate predictive model but instead focuses on understanding the dynamics within $\mathbb{A}_{\mathbb{D}}$ using neural network. A notable advantage of machine-learning models is their ability to weakly model dynamics that are not necessarily closed. In this study, we attempt to apply these methods to map A_I, A_O, A_P onto $\mathbb{A}_{\mathbb{D}}$. In addition, although the dynamics of a flow field and points in the state space $\mathbb{J}$ constitute high-dimensional dynamics,[24] they are reduced to three dimensions within $\mathbb{A}_{\mathbb{D}}$. Each orientation governed by $\mathbb{U}$ evolves independently without interference, and the resulting distribution of orientations and the flow field exhibit a certain type of high-dimensional dynamics. If this behavior can be effectively modeled in the three-dimensional space, it suggests that the essential information of the high-dimensional dynamics can be projected onto a lower-dimensional representation for modeling or mathematical formulation.

When the dynamics are not closed, the maps A_I, A_O, and A_P do not become injective. In such cases, an examination of the model's adaptability is performed. Specifically, the analysis is performed regarding the shear history, as described by Eq.(9). The time evolution of I, O, and P within the shear history space $\mathbb{A}_{\mathbb{D}}$ is expressed in terms of the features ω_1 and ω_2, and the following map A_I is introduced (similarly for A_O and A_P):

$$A_I : \begin{pmatrix} I(t) \\ O(t) \\ P(t) \\ \omega_1 \\ \omega_2 \end{pmatrix} \mapsto \dot{I}(t). \tag{11}$$

We define ω_1 and ω_2 as path information representing the features of the flow field at time t. These quantities are determined at each time step based on the path and do not describe the dynamics. Additionally, the model constructed in this study does not strictly consider the entire history and differs from learning models such as LSTM and DSDL[20] for handling time-series data. While approaches that consider history are well suited for time-series analysis, this study focuses on the analysis of physical dynamics. Therefore, a method that uses only the features at each time step was adopted, as shown in Eq.(11).

In this study, the shear history space $\mathbb{A}_{\mathbb{D}}$ was divided into training, validation, and test datasets and an analysis was performed. The results revealed that the learning efficiency, learning adaptability, and adaptability when using the test data vary significantly depending on $\mathbb{A}_{\mathbb{D}}$. This variation is thought to correspond to the complexity of the dynamics within the flow field. In this section, we evaluate these effects quantitatively and discuss the applicability of the learning model.

4.2.1 Model Design

A simple regression model consisting of linear layers with 125 units and tanh activation functions was created for the mappings A_I, A_O, A_P (FIG.12).[25] The neural network consists of two parallel linear layers, each processing one of the input feature datasets. The first layer, which receives the (I, O, P) input, has 125 hidden units with tanh activation. The second layer, which processes the shear parameters (ω_1, ω_2), also consists of 125 hidden units with tanh activation. These outputs are combined and input directly into the final output layer (1

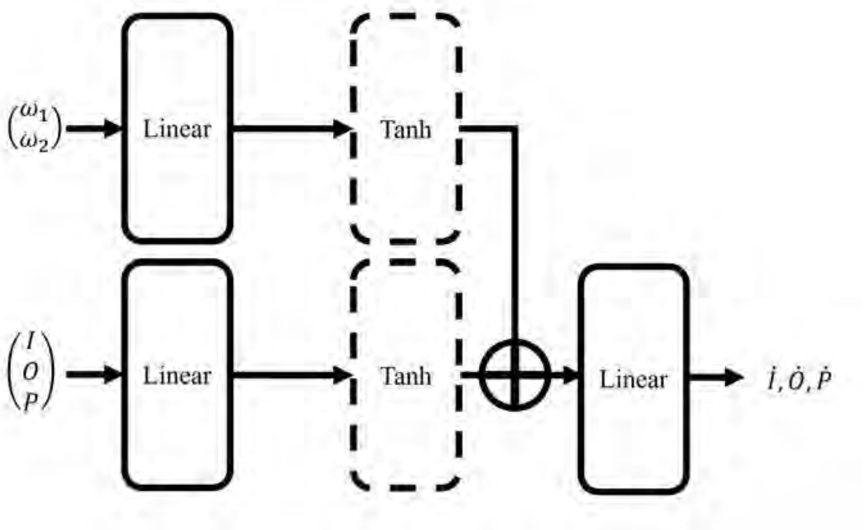

Fig. 12. Neural network model featuring a linear layer followed by the tanh activation function.

unit). The reasons for selecting this model are as follows:

- The contribution of ω_1 and ω_2 to the temporal evolution of $I(t), O(t), P(t)$ is expected to be nonlinear. Therefore, tanh was introduced to appropriately capture this nonlinearity. However, nonlinear effects between ω_1, ω_2 and $I(t), O(t), P(t)$ were not included.
- The simplicity of the model structure improves computational efficiency.

Furthermore, the mean squared error (MSE) was employed as the loss function, and the model was trained to optimize the prediction errors of $\dot{I}(t), \dot{O}(t), \dot{P}(t)$.

4.2.2 Preprocessing of the Dataset

We investigated seven shear history spaces denoted as $\mathbb{A}_{\mathbb{D}_{\omega_1,\omega_2}}$. The quantities I, O, P were computed with a time step of $\Delta t = 10^{-4}$ up to $t = 10$, and the data sampled at intervals of 10^{-3} were used for the analysis. For each shear history space, the datasets were partitioned sequentially at a ratio of 80:10:10 into training, validation, and test sets.

Furthermore, the temporal evolution of I, O, P is expected to exhibit varying scales. The application of preprocessing methods such as min–max normalization across the entire dataset would introduce statistical information from the entire $\mathbb{A}_{\mathbb{D}_{\omega_1,\omega_2}}$, potentially incorporating future data. To prevent this, scaling was performed using only the minimum and maximum values within the training dataset. This is the only preprocessing applied to the datasets. Each dataset consists of two sets of input features: (i) the physical quantities I, O, P, represented as a matrix of shape $N \times 3$, where N is the batch size; and (ii) the shear parameters (ω_1, ω_2), represented as $N \times 2$. These inputs are fed into two separate linear layers for processing.

4.2.3 Training and Validation

The Adam optimizer was used for training with a learning rate of 10^{-2} and batch size of 32. Random batches were created from the training data every 100 epochs and training was performed for a fixed maximum of $10,000$ epochs to compare the learning rates in each space. In addition, validation was conducted every 20 epochs using the training data, and early stopping was applied if the validation error did not improve for 10 consecutive epochs.

To examine the sensitivity of the model to hyperparameters, we conducted additional experiments by varying the number of hidden units $(60, 125, 250)$, and batch sizes $(16, 32, 64, 128)$. As a result, increasing the number of hidden units beyond 125 did not lead to significant improvements in accuracy, and similar trends were observed with larger batch sizes. Furthermore, there was almost no variability in the results, indicating stable learning outcomes with this setting. All of these results were validated using the validation dataset of shear history space $\mathbb{A}_{\mathbb{D}_{0,4\pi}}$, suggesting that a hidden unit count of 125 and a batch size of 32 are effective in balancing accuracy, stability, and computational cost. (FIG. 13)

4.2.4 Testing and Performance Evaluation

The performance of the final model was evaluated using the test data. MSE was used as the evaluation metric. The differences between the training and test errors and variations in errors across different spaces were thoroughly examined, and their respective impacts were analyzed.

4.2.5 Performance Analysis

In addition to the cases illustrated in FIG.4A–E, we extended our analysis to include two additional shear history spaces, $(\omega_1, \omega_2) = (8\pi, 2\pi)$ and $(5\pi, 7\pi)$ (FIG.14), resulting in a total of seven different shear history spaces $\mathbb{A}_{\mathbb{D}_{\omega_1,\omega_2}}$. We evaluated the mappings A_I, A_O, A_P in these spaces; the MSE for each test dataset is summarized in TABLE I and FIG.15. The horizontal axis represents the three mappings A_I, A_O, A_P, whereas the vertical axis represents the common logarithm of the MSE.

For A_I (black points in FIG.15), it was observed that the error increases as the trajectory becomes more complex. While there was little variation in the error for the validation dataset of $\mathbb{A}_{\mathbb{D}_{0,4\pi}}$, substantial variation was observed when evaluating with the test dataset. Next, for A_O(red squares in FIG.15), since the indicator P is provided as an input, no significant dif-

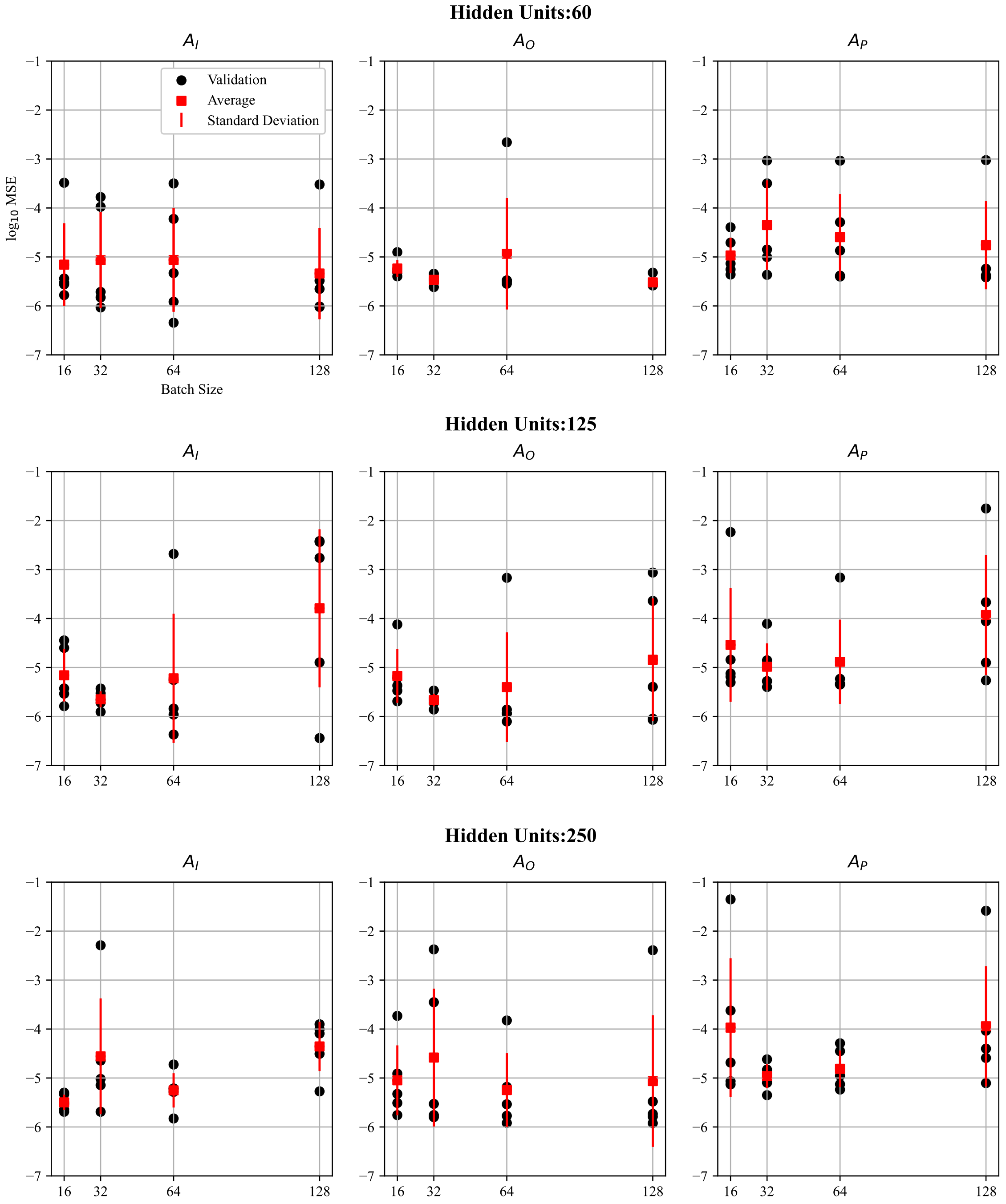

Fig. 13. Sensitivity analysis of the model to hyperparameters. The mean squared error (MSE) of A_I, A_O, A_P was evaluated on the validation dataset of shear history space $\mathbb{A}_{\mathbb{D}_{0,4\pi}}$ for each combination of hidden layer units $(60, 125, 250)$ and batch sizes $(16, 32, 64, 128)$. Five trials were conducted for each setting, with the results represented by black points. The mean values across the five trials are shown as red squares, with error bars indicating the standard deviation.

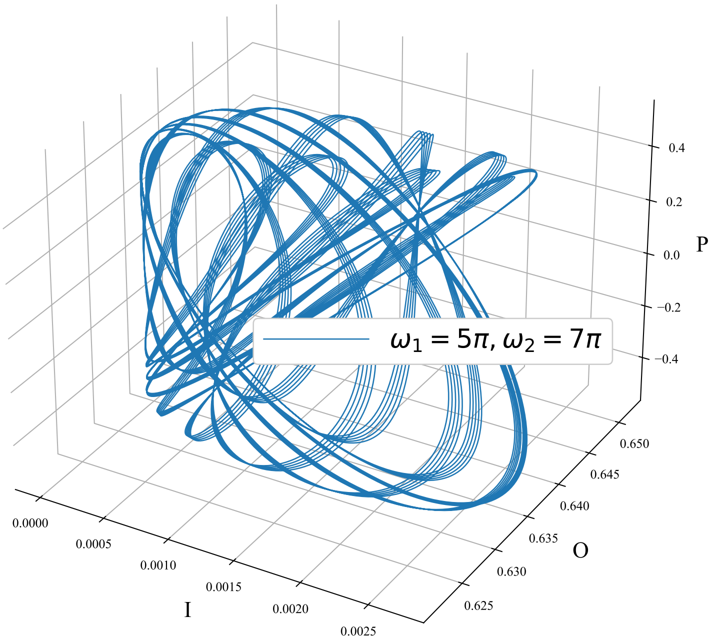

Fig. 14. Time evolution of I, O, and P in $\mathbb{A}_{\mathbb{D}_{5\pi,7\pi}}$.

ferences were observed across all $\mathbb{A}_{\mathbb{D}_{\omega_1,\omega_2}}$, confirming stable learning. In contrast, A_I and A_P exhibited an increasing error correlated with the complexity of the trajectory. Particularly, for $(\omega_1, \omega_2) = (8\pi, 4\pi)$, where a limit cycle is formed in the O–P plane, the sharp variation in P at $O = 0$ caused an outlier-like distribution of data, leading to an increased MSE for both A_O and A_P. Finally, for A_P(blue triangles in FIG.15), differences were observed between $(\omega_1, \omega_2) = (0, 0)$, $(0, 4\pi)$, $(2\pi, 0)$ and $(\omega_1, \omega_2) = (8\pi, 4\pi)$, $(5\pi, 5\pi)$, $(8\pi, 2\pi)$, $(5\pi, 7\pi)$. These differences are also likely associated with the complexity of the trajectory.

In this study, hyperparameter selection was conducted using the validation data for $(\omega_1, \omega_2) = (0, 4\pi)$. However, to achieve a more general tuning process, data from multiple spaces should be used. The effects of significantly increasing the number of hidden units and expanding the batch size were examined to see if they would improve the latter results, but no significant improvement was observed. This result highlights the limitations of a simple neural network model. In particular, as shown in the FIG.16, A_I failed to learn effectively

Table I. MSE for the test dataset

(ω_1, ω_2)	$\log_{10}\mathrm{MSE}(A_I$ test)	$\log_{10}\mathrm{MSE}(A_O$ test)	$\log_{10}\mathrm{MSE}(A_P$ test)
$(0, 0)$ (FIG.4A)	-6.958 ± 0.347	-6.427 ± 0.336	-4.379 ± 1.120
$(0, 4\pi)$ (FIG.4B)	-4.791 ± 1.586	-5.798 ± 0.153	-4.278 ± 1.148
$(2\pi, 0)$ (FIG.4C)	-3.586 ± 0.114	-5.877 ± 0.072	-5.194 ± 0.096
$(8\pi, 4\pi)$ (FIG.4D)	-3.274 ± 0.552	-3.168 ± 0.041	-2.382 ± 0.023
$(5\pi, 5\pi)$ (FIG.4E)	-1.463 ± 0.232	-5.345 ± 0.076	-2.015 ± 0.282
$(8\pi, 2\pi)$	-2.178 ± 0.081	-5.088 ± 0.076	-2.177 ± 0.214
$(5\pi, 7\pi)$ (FIG.14)	-1.172 ± 0.038	-4.998 ± 0.165	-1.973 ± 0.022

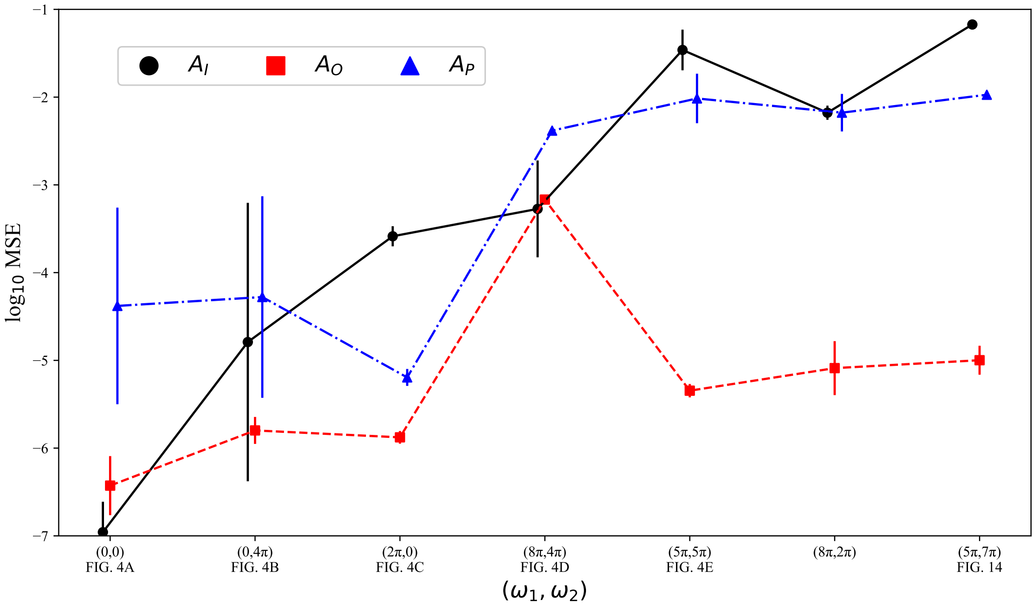

Fig. 15. Mean squared error (MSE) of A_I, A_O, A_P evaluated on the test dataset. Test results for various shear history spaces $\mathbb{A}_{\mathbb{D}_{\omega_1,\omega_2}}$. Black points represent A_I, red squares represent A_O, and blue triangles represent A_P. Error bars indicate the standard deviation.

even for the both training and test datasets in the trajectory at $(\omega_1, \omega_2) = (5\pi, 7\pi)$. The absence of nonlinear effects between (I, O, P) and (ω_1, ω_2) is likely a key factor underlying this limitation.

These findings suggest that the learning difficulty varies depending on the trajectory structure within $\mathbb{A}_{\mathbb{D}_{\omega_1,\omega_2}}$. Specifically, the trajectory in the case of $(\omega_1, \omega_2) = (5\pi, 7\pi)$ may exhibit an irregular behavior. (FIG.14). In the model used in this study, certain trajectories could not

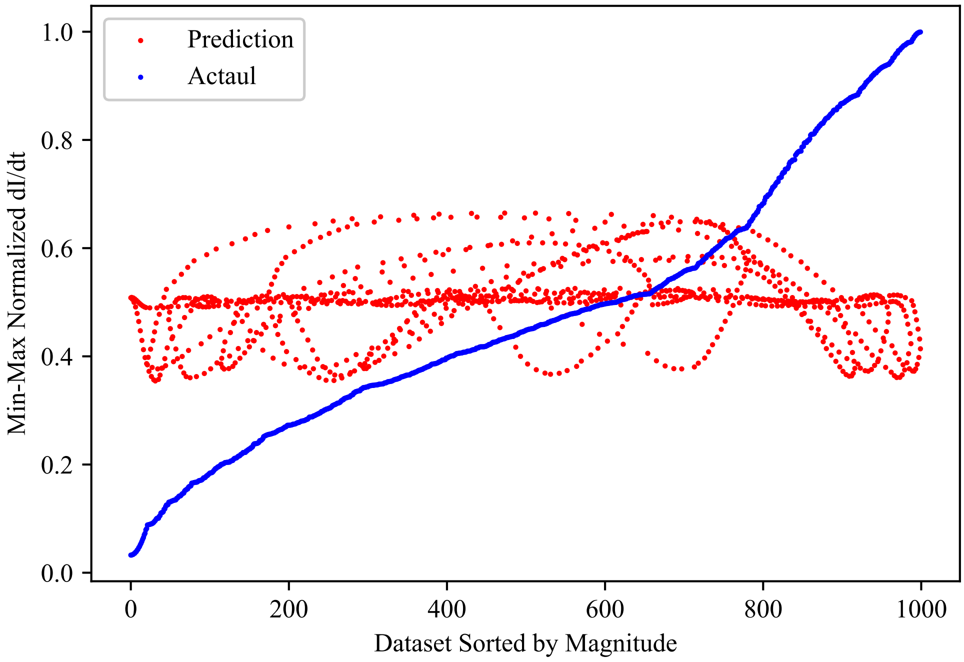

Fig. 16. Prediction results for A_I at $(\omega_1, \omega_2) = (5\pi, 7\pi)$. The test dataset, normalized by Min-Max scaling, is sorted in ascending order. The blue points represent the actual values, while the red points represent the predicted values. A similar trend is observed in the training data, indicating that the model has not learned effectively.

be learned effectively from the training data. Although this may be attributed to factors such as the simplicity of the model or the size of the datasets, it is also likely that the learning challenge arises from the strong sensitivity to the position within $\mathbb{A}_\mathbb{D}$. This suggests that when considering non-closed dynamics within $\mathbb{A}_\mathbb{D}$, the system may exhibit chaotic-like behavior. It also suggests that the entire system dynamics including these phenomena can be efficiently categorized.

The model proposed here is relatively simple, and particularly, there is no nonlinear relationship between the features input into the separate parallel linear layers. However, certain trajectories within specific shear history spaces can be predicted with high accuracy, which suggests that a mathematical formulation may be possible within these spaces. Conversely, as the complexity of the trajectories increases, the accuracy decreases, and in cases of more complex trajectories, the model failed to learn effectively. Keeping this in mind, improvements to the model and further evaluation will be necessary in future work.

5. Summary

Optical visualization using flakey particles is a well-established technique for visualizing flow. However, the specific flow information conveyed by the light and dark patterns produced through this method remains unclear. These patterns exhibit a strong correlation with the orientation distribution of flakey particles in the local region (POD). Therefore, the objective of this study was to investigate the dynamics of POD within the flow field. First, this study introduces a shear history space $\mathbb{A}_{\mathbb{D}}$ from a set-theoretic perspective to reduce the dimensionality of POD motion in a flow field and enhance its interpretability. Next, attractors, periodic trajectories, and limit cycles were identified within the shear history space, suggesting the potential to extract shear and periodicity from the flow. When attractors are present or when limit cycles form in the $O - P$ plane, the shear direction in the flow can be fully determined. We also showed in Section 4-1 that if there is a specific situations in the shear history space $\mathbb{A}$, then by doing the two conjectures appropriate from the visualization experimenter's standpoint, that the shear direction can be determined. However, the applicability of optical visualization techniques for measuring shear in fluid flows using flakey particles is significantly constrained. Furthermore, experimenters face substantial challenges in correctly identifying actual flow situations based on brightness. Additionally, the analysis conducted in this study was based on specific trajectories, and in actual visualization experiments, combinations of diverse trajectories in 3D space affect the outcomes. Therefore, it is crucial not only to focus on the analysis of infinitesimal regions but also to deepen our understanding of local spatial regions, as this will be important for interpreting the flow field information obtained from visualization experiments using flakey particles.

Furthermore, this study analyzed non-closed dynamics using a simple neural network model, providing a new perspective on the relationship between POD and the flow field. Although the model achieved a certain level of adaptability for attractors and periodic orbits, the results revealed the influence of trajectory complexity on learning performance. This finding suggests the potential for quantifying chaotic-like or irregular trajectories. The proposed model is simple, with no nonlinear relationships between features in the parallel linear layers. It predicts certain trajectories accurately, suggesting a possible mathematical formulation within these spaces. However, performance decreases with increasing trajectory complexity, and the model fails to learn in more complex cases. Future work should focus on model improvements, further evaluation and mathematical formulation.

These results of this study provide a new perspective on analyzing the relationship between the distribution and statistical properties of particles and the governing law that dictates their motion when all particles follow a common governing principle. The proposed approach expands the interpretation of particle visualization in fluid dynamics and offers a novel framework for achieving a deeper understanding of the dynamics, paving the way for further applications in this field.

A future challenge is to develop a framework for understanding POD dynamics within the entire physical space, which is formed by integrating and synthesizing all shear history spaces generated by a given flow, in terms of actual optical visualization experiments using flakey particles.

Acknowledgment

This work was supported in part by a Grant-in-Aid for Scientific Research(C) and JSPS KAKENHI Grant No.24K07331 and by the Kansai University Grant-in-Aid for progress of research in graduate course, 2024. The authors would like to thank Mr. Yoshikawa for his valuable comments on the draft. They also acknowledge ORDIST in Kansai University and the RIMS Joint Research Activities in Kyoto University for providing a space for their research and communication.

References

1) M. V. Dyke, *An Album of Fluid Motion.* Parabolic press, Stanford, California, 1982.

2) L. P. Sung, M. E. Nadal, M. E. McKnight, E. Marx, and B. Laurenti, “Optical reflectance of metallic coatings: Effect of aluminum flake orientation,” *Journal of Coatings Technology*, vol. 74, pp. 55–63, 2002.

3) G. Gauthier, P. Gondret, and M. Rabaud, “Motions of anisotropic particles: application to visualization of three-dimensional flows,” *Physics of Fluids*, vol. 10, no. 9, pp. 2147–2154, 1998.

4) G. B. Jeffery, “The motion of ellipsoidal particles immersed in a viscous fluid,” *Proceedings of the Royal Society of London. Series A, Containing papers of a mathematical and physical character*, vol. 102, no. 715, pp. 161–179, 1922.

5) Ö. Savaş, “On flow visualization using reflective flakes,” *Journal of Fluid Mechanics*, vol. 152, pp. 235–248, 1985.

6) S. Kida, “Theoretical prediction of a bright pattern of reflective flakes in a precessing sphere,” *Fluid Dynamics Research*, vol. 46, no. 6, p. 061404, 2014.

7) S. Goto, *Visualization of Turbulence by Using Reflective Flakes.* Kashikazy-ouhouGakaishi, 2019, vol. 34.

8) C. Egbers and H. J. Rath, “The existence of taylor vortices and wide-gap instabilities in spherical couette flow,” *Acta Mechanica*, vol. 111, pp. 125–140, 1995.

9) K. Yoshikawa, T. Itano, and M. Sugihara-Seki, “Numerical reproduction of the spiral wave visualized experimentally in a wide-gap spherical couette flow,” *Physics of Fluids*, vol. 35, no. 3, 2023.

10) I. Arai, T. Itano, and M. Sugihara-Seki, “Revisiting visualization of spiral states in a wide-gap spherical couette flow,” *Acta Mechanica*, vol. 235, no. 12, pp. 7441–7452, 2024.

11) I. Arai, K. Yoshikawa, and T. Itano, “Puseudo-visualization and analysis of phase in two-dimensional flow using aluminium flake tracers,” *SCIENCE and TECHNOLOGY REPORTS of KANSAI UNIVERSITY*, vol. 67, pp. 21–28, 2025.

12) G. K. Batchelor, *An introduction to fluid dyanmics.* Cambridge, UK: cambridge university press, 1967.

13) S. Goto, S. Kida, and S. Fujiwara, “Flow visualization using reflective flakes,” *Journal of fluid mechanics*, vol. 683, pp. 417–429, 2011.

14) K. Bingi, P. A. M. Devan, and F. A. Hussin, “Reconstruction of chaotic attractor for fractional-order tamaševičius system using recurrent neural networks,” in *2021 Australian & New Zealand Control Conference (ANZCC)*. IEEE, 2021, pp. 1–6.

15) M. Reichstein, G. Camps-Valls, B. Stevens, M. Jung, J. Denzler, N. Carvalhais, and F. Prabhat, “Deep learning and process understanding for data-driven earth system science,” *Nature*, vol. 566, no. 7743, pp. 195–204, 2019.

16) Z. M. Zhai, M. Moradi, L. W. Kong, B. Glaz, M. Haile, and Y. C. Lai, “Model-free tracking control of complex dynamical trajectories with machine learning,” *Nature communications*, vol. 14, no. 1, p. 5698, 2023.

17) C. J. Lagares, S. Roy, and G. Araya, “An algebraic domain reprojection, deep learning and dns-data-driven approach for turbulence modeling,” in *AIAA SCITECH 2025 Forum*, 2025, p. 0697.

18) S. L. Brunton, B. R. Noack, and P. Koumoutsakos, “Machine learning for fluid mechanics,” *Annual review of fluid mechanics*, vol. 52, no. 1, pp. 477–508, 2020.

19) T. Ma, H. Chen, K. Zhang, L. Shen, and H. Sun, “The rheological intelligent constitutive model of debris flow: A new paradigm for integrating mechanics mechanisms with data-driven approaches by combining data mapping and deep learning,” *Expert Systems with Applications*, vol. 269, p. 126405, 2025.

20) M. Wang and J. Li, “Interpretable predictions of chaotic dynamical systems using dynamical system deep learning,” *Scientific Reports*, vol. 14, no. 1, p. 3143, 2024.

21) B. Ramadevi and K. Bingi, “Chaotic time series forecasting approaches using machine learning techniques: A review,” *Symmetry*, vol. 14, no. 5, p. 955, 2022.

22) A. Abbas, H. Abdel-Gani, and I. S. Maksymov, “Edge-of-chaos and chaotic dynamics in resistor-inductor-diode based reservoir computing,” *IEEE Access*, 2025.

23) F. Petropoulos, D. Apiletti, V. Assimakopoulos, M. Z. Babai, D. K. Barrow, S. B. Taieb, C. Bergmeir, R. J. Bessa, J. Bijak, J. E. Boylan *et al.*, “Forecasting: theory and practice,” *International Journal of forecasting*, vol. 38, no. 3, pp. 705–871, 2022.

24) P. R. Vlachas, W. Byeon, Z. Y. Wan, T. P. Sapsis, and P. Koumoutsakos, “Data-driven forecasting of high-dimensional chaotic systems with long short-term memory networks,” *Proceedings of the Royal Society A: Mathematical, Physical and Engineering Sciences*, vol. 474, no. 2213, p. 20170844, 2018.

25) K. Saito, *Zerokaratukuru Deep Learning*. O’ Reilly Japan, vol. 1,2,3.